國立臺灣大學理學院物理學研究所

碩士論文

Graduate Institute of Physics

College of Science

National Taiwan University

Master Thesis

使用微中子望遠鏡的前端讀出系統做單光子之量測

The Single Photon Measurement by Using The Front-End

Readout System of Neutrino Telescope

張智堡

Chih-Pao Chang

指導教授：王名儒 教授

Advisor: Min-Zu Wang, Prof.

中華民國一百年六月

6, 2011

誌謝

　　首先，我要感謝我的指導老師—王名儒教授，您耐心地帶領我進入高能粒子物理實驗的領域並且指引我正確的研究方向，培養我解決問題的能力。 感謝上野耕資教授總是能在每次開會給予我很多意見，尤其在於研究上的堅持是令我敬佩的。 感謝徐靜戈博士也教導了我許多電子電路的知識，幫助我解決很多硬體上的問題。 感謝黃坤賢總是不厭其煩地和我討論問題，這篇論文大部分的基礎知識都是從你那裡學習來的。 我要感謝在NuTel計畫中一起合作的研究人員：李俊霖、張硯詠、周建宏、范若妤、蕭成翰、廖冠豪，沒有你們的協助及建議，我無法順利地完成我的研究。 感謝在研究所又相遇的大學同學何泰祥，雖然你常常有很多無厘頭的想法，我們也常互相吐槽，但感覺的到你最常關心朋友。 張佑豪總是實驗室歡樂的來源，感謝你讓我在實驗室找到臭味相投的夥伴，你去歐洲的那一年，實驗室失色了許多。不過我知道你在歡笑的外表底下卻是有一顆縝密的心思。 陳柏元、董育宸、董彥瑋、彭政傑、徐嘉伶、許祖達、杜伊婷、吳姿瑩、Charles、賴加翌、沈家賢以及其他高能物理實驗室成員，感謝有你們的研究所的時光能和你們相處，一起學習、互相關心、聊天、抱怨，沒有你們，我想實驗室的生活可能就乏味許多。

　　棒球是我最愛的運動，我要感謝過去在球場上一起奮戰的清物系棒的夥伴們，我們沒那麼厲害，但我們曾打出一場場好比賽。 在研究之外，我也參與了一個社團— Pangcah阿美族守護聯盟，舉辦了幾場記者會及抗議活動，為了爭取Pangcah的權益。感謝這些夥伴們讓我更加地認識自己的族群，也激發起我的自我意識。

　　感謝我的部落—Makota'ay（港口部落），也感謝部落裡很多親朋好友的鼓勵，雖然我從研究所畢業了，但在部落裡面的文化、學問，我才剛剛起步在學習。感謝Palalanay（巴拉拉奈）裡所有的slarl，大家的團結讓我每年都很感動，身為其中的一份子，我感到很榮幸。感謝拉清寒階級的各位朋友—Daong、Fotol、Langus、Sra、Hafay、Laway，讓我在台北這大都市，還能過

i

著Pangcah的生活。 感謝新店溪洲部落的族人們，你們讓我知道原來在台北還有那麼像原鄉部落的地方，你們熱情的對待，讓我像是回到花蓮一般。更重要的，在這美麗的地方，我認識了我的女朋友。

最後感謝我的家人。 感謝爸爸總是在背後支持著我，自由地讓我自己發揮想做的事，從不會要求成績要多好，唯一只要求我要有健康的身體。 感謝媽媽很辛苦地將我撫養長大，即使生活如何困苦，為了我和妹妹，還是堅強地撐過去。我長大了，會讓妳減輕負擔，也同時希望我能不負妳的期望。 感謝我的妹妹，雖然和妹妹因為求學分隔兩地，見面的時間不多，但相聚時總是會歡笑不斷。 感謝我的外婆，遇到重要事情時，總是會為我禱告；您為我做的Opih（羽冠）是全村最漂亮的，我知道您對我的期待很高，我也會好好練習Pangcah。 感謝我的女朋友─易蓉（Tipus），總是包容著我的粗心，在妳的旁邊，我常常像個小孩一般。 我很欣賞妳那強烈的正義感跟責任感，這也改變了我許多，雖然我常常很擔心妳的正義感會不會出事。 過去我有很多想法沒有去執行，妳總是會在我身旁鼓勵我，甚至協助我去完成。 妳影響了我很多，沒有妳，我想我走的路將會完全不同。 很感謝有妳三年多來的陪伴。

在撰寫這篇論文時，奶奶過世了，很遺憾沒能讓您看到我跨越人生的另一個階段，因此，希望您在天上能分享我的榮耀。 外公是我崇拜的人，不論是上山下海，甚至是讀書考試，都樣樣精通。從小你不斷著叮嚀著我「要好好讀書」，媽媽說這是你當年的遺憾，現在我拿到碩士學位了，希望我沒有辜負Kacaw這個和您相同的名字。

最後，僅以此論文獻給兩個人─奶奶和外公。

張智堡(Kacaw·Kaokoy·Cikatopay)

2011.08.03

摘要

台灣大學高能實驗室的微中子望遠鏡（NuTel）是一個利用擦射地球法（Earth-skimming technique）來觀測陶子微中子（ν_τ）的偵測器，當陶子微中子（ν_τ）與地表起作用會產生陶子（τ）。而微中子望遠鏡主要是觀測高能量陶子產生的契倫諧夫光（Cherenkov light）來作為偵測到陶子微中子的證據。因此，微中子望遠鏡的光度校正是非常重要的。

這篇論文主要集中於單光子量測。我們利用微中子望遠鏡的電子前端讀出系統來觀測單光電子，藉由三種方法，我們成功地量測到單光電子相對應的數位量值。另外，我們組裝了一個可達一萬伏特的高壓電源供應器來供給hybrid photodetector (HPD)，並且利用HPD，我們成功地觀測到單光電子的峰值，證實微中子望遠鏡的電子前端讀出系統所量出的結果。

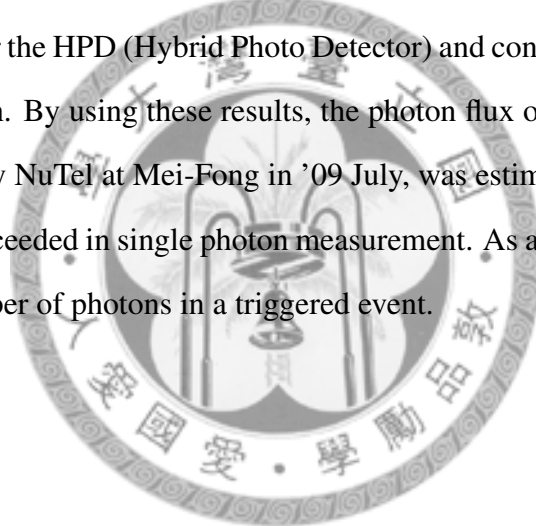利用以上的光度校正數據，我們可以估算微中子望遠鏡所收集的光子數。而在2009年夏天，我們在梅峰進行了夜間天空背景量測（night sky background），估算出其光通量。

至今，電子前端讀出系統已成功觀測到單光電子。因此，微中子望遠鏡有能力估計量測到的光子數量。

iii

Abstract

NuTel (Neutrino Telescope) is a detector to detect the tau neutrino ν_τ with the earth skimming technique. Through mountains, ν_τ converts to τ leptons. NuTel is designed to observe the Cherenkov light from the air shower that produced by high energy τ leptons. For the NuTel experiment, the calibration of the brightness measurement is important.

This thesis focuses on the single photon measurement. We used the electronic read-out systems of NuTel to observe single photoelectron. By three kinds of methods, we got the digitized value corresponds to the single photoelectron. Furthermore, we made a 10kV power supply for the HPD (Hybrid Photo Detector) and confirmed the measurement of single photoelectron. By using these results, the photon flux of night sky background, which was observed by NuTel at Mei-Fong in '09 July, was estimated.

So far, NuTel succeeded in single photon measurement. As a result, NuTel is capable of measuring the number of photons in a triggered event.

Contents

List of Figures

List of Tables

Chapter 1

Introduction

1.1 Physics

Neutrinos play important roles in particle physics. Except gravitation, which is too weak to be considered, neutrinos are only affected by weak interaction. Because their cross-section is small and mass is light, they hardly interact with the matter as they travel through universe. Thus, it could directly point to the site of production of energetic particles.

Neutrinos may come directly from sources like Active Galactic Nuclei (AGN), Gamma Ray Bursts (GRB) or the Galactic Center (GC), or be produced when the cosmic ray interacts with the galactic disc. Generally, cosmic rays hitting matter would produce pions as the reation: [1]

$$p + p \rightarrow p + n + \pi^+.$$
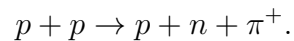
The charged pion decay predominantly by the reaction: [1]

$$\pi^+ \rightarrow \mu^+ + \nu_\mu$$
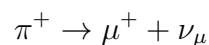
The muon decay is as following: [1]

$$\mu^+ \rightarrow e^+ + \nu_e + \bar{\nu}_\mu$$
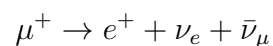
So the ratio of $\nu_e : \nu_\mu : \nu_\tau \simeq 1 : 2 : 0$ when they are originally produced in the universe. However, with the maximum oscillation taking place, the ratio of $\nu_e : \nu_\mu : \nu_\tau \simeq 1 : 1 : 1$ [2]. Detecting a τ lepton descendent on Earth would not only probe AGN/GRB/GC mechanisms, but would also constitute a ν_τ-appearance experiment.

1.2   NuTel Project

Neutrino experiments need a large taget volume to convert incoming neutrinos into detectable objects like charged leptons or proton recoil for observation. The NuTel build a wide field-of-view Cerenkov telescope and use earth-skimming method to observe air shower behind a mountain. Only the τ lepton has a reasonable probability to escape the mountain and initiate extensive air showers. In this technique, the energy range of ν_τ is from 1 PeV to 1000 PeV [3], and the most suitable source are AGNs [4]. Shiang-Rung Tsai had estimated the sensitivity of NuTel [5]. With such a sensitivity, NuTel can be used for searching the AGN neutrino with maybe one event per three years.

1.3   Single Photon Measurement

NuTel observes air shower to detect ν_τ, so the energy reconstruction depends on light intensity. Thus, to estimate the collected light is important. The photodetector in NuTel is Multi-Anode Photo-Multiplier Tube (MAPMT). It has fast time response and good position resolution. The goal of this research is to measure single photoelectron to calibrate gain factor.

In Chapter 2, we introduce our NuTel apparatus. The signal we receive is analog-to-digital converter (ADC). In Chapter 3 It is mentioned that reconstruct MAPMT's charge signal from ADC. We present the calibration method of MAPMT and count photoelectron with LED light in Chapter 4. Chapter 5 shows the observation of HPD and the result of comparison with MAPMT. The Night Sky Background measurement in Mei-Fong is

shown in Chapter 6.

Chapter 2

NuTel Apparatus

2.1 Introduction

For the purpose of observing air showers behind mountains, NuTel has to be built with wide field of view optics system and fast electronics readout system. The sources of the air showers is tau(τ).

Figure 2.1 is the schematic of NuTel apparatus. The apparatus of NuTel consists of optics system and front-end readout system. Our optics system adopts Schmidt mirror system, which has $8° \times 8°$ field of view (FOV). It focus Cerenkov light, whose wavelength is from 350 nm to 450 nm, on surface of MAPMT. The front-end readout system includes MAPMT, Pre-amp, DCM, and DAQ. MAPMT coverts the collected light into charge (current) signal. Because it has 64 pixels, it provides space discrimination. The charge signal is sent to Pre-amp, and Pre-amp convert current pulse into differential voltage signal. DCM receives voltage signal and then digitizes it with 10-bit 40MHz ADC. DCM has trigger FPGA to decide which event should be triggered. The triggered event is saved in 32-event size Buffer RAM. When 16 triggered events are saved in Buffer RAM, the Master DCM send an interrupt into SBC. As a result, 16 events in DCM are transfered via CompactPCI buses to save into hard disk in SBC.

One telescope apparatus

8x8 =64 pixels
PMT x8

Light-guide   MAPMT

Preamp.

16 channels
Pre-amp x32

Reflective
Mirror

HV power
supply
in VME

Trigger
daisy
chain

Trigger
FPGA

start readout

potentio-
meter

2m

cable

DAQ

cPCI
bus

buffer
RAM

cycle
RAM

ADC

10-bit ADC

32 channels DCM x16
in c-PCI
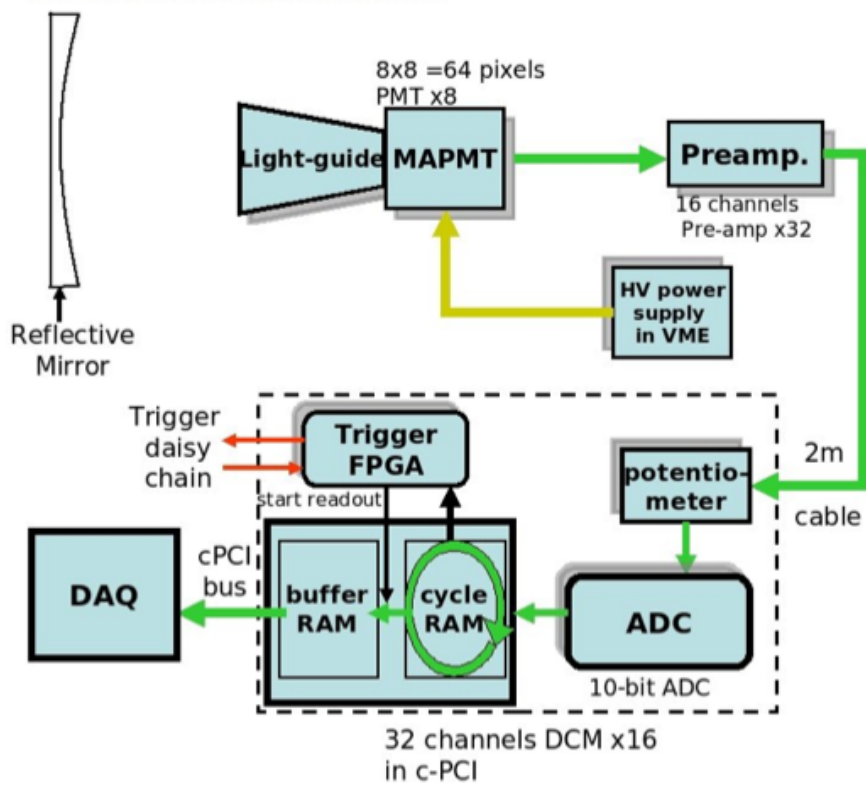
Figure 2.1: One telescope schematic

2.2 Optics System

For the purpose of collecting Cerenkov light to detect the tau neutrino (ν_τ), a large field of view (FOV) of optics is needed. The Schmidt mirror system is adopted as the optical system [6]. Its FOV is $8.92°$. Figure 2.2 shows a schematic of a Schmidt telescope. In Schmidt optical system, the mirror is spherical. Therefore, it is free of chromatic aberration but it suffers spherical aberration. To reduce spherical aberrations, a aspherical correction lens is added in front of the spherical mirror. Thus, the light is collected on a curved image surface. Figure 2.3 shows the spot size in different angles and different wavelength of lights. The spectral response of MAPMT is from 300nm to 650nm, but the wavelength of Cerenkov light we want to capture is from 350nm to 450nm. Thus, BG3 filters, which are UV band-passing filters, are used in front of surface of MAPMT. Figure 2.4 shows BG3 and Figure 2.5 shows the graph of transmittance to wavelength.
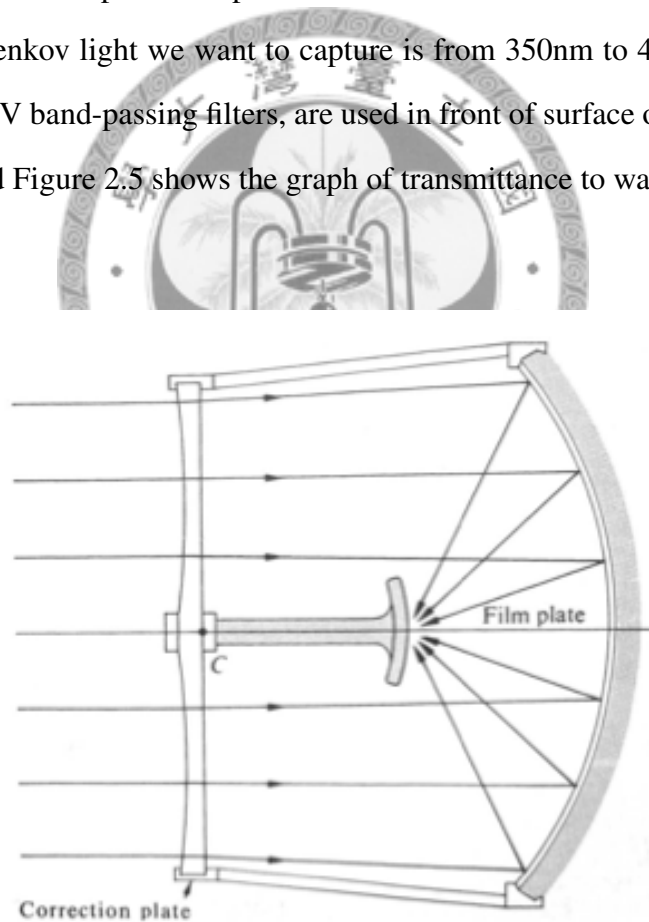
Figure 2.2: Schematic of a Schmidt telescope [7]
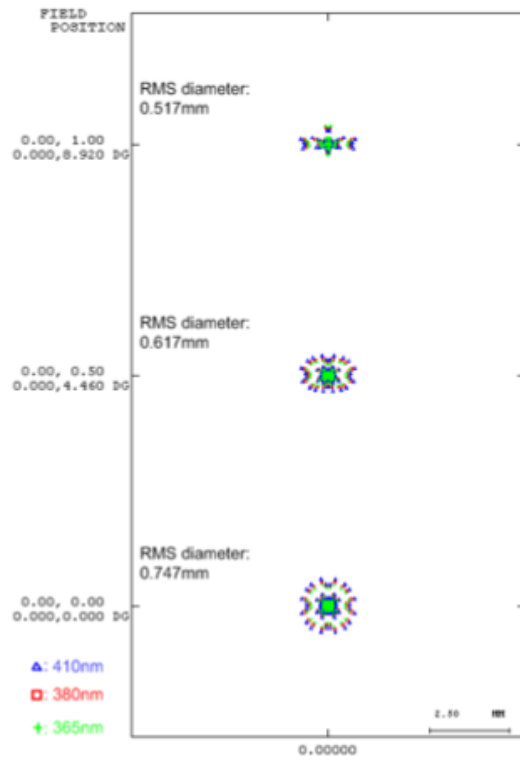
Figure 2.3: The spot diagram of a curved image surface [6]
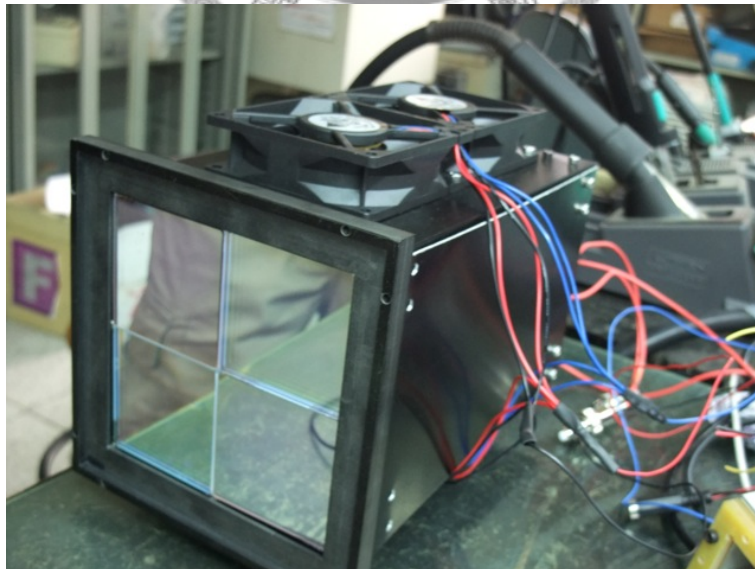
Figure 2.4: A frame of 4 MAPMTs and there are 4 BG3 in front of frame.
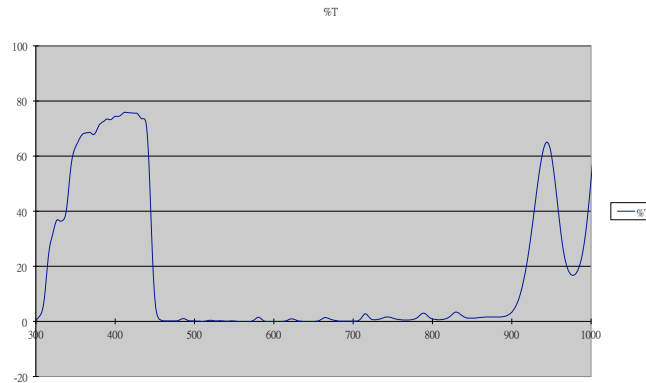
Figure 2.5: The graph of transmittance to wavelength of BG3

2.3 Front-End Readout System

The front-end readout system of NuTel consists of MAPMT, Pre-amp, DCM, DAQ. The photons which are collected by optic system hit photocathode on the surface of MAPMT, and then the photoelectrons are produced. Through several dynodes, the multiplied secondary electrons collected by the anode.

2.3.1 Multi-Anode Photo Multiplier Tubes (MAPMT)

Principle

A photomultiplier tube (PMT) is a vacuum tube consisting of an input window, a photocathod, focusing electrodes, an electron multiplier and an anode usually sealed into an evacuated glass tube. Figure 2.6 shows the schematic construction of a photomultiplier tube.

Light which enters a PMT is detected and produces an output signal through the following processes.

(1) Light passes through the input window.

9
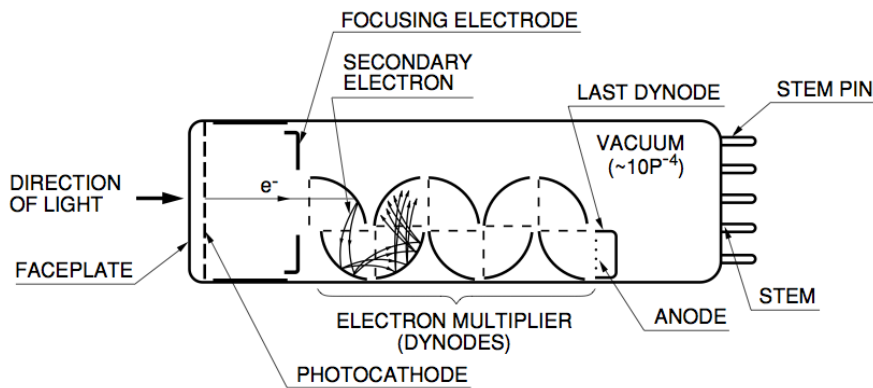
Figure 2.6: Construction of a photomultiplier tube [8]

(2) Light excites the electrons in the photocathode so that photoelectrons are emitted into the vacuum (photoelectric effect).

(3) Photoelectrons are accelerated and focused by the focusing electrode onto the first dynode where they are multiplied by means of secondary electron emission. This secondary emission is repeated at each of the successive dynodes.

(4) The multiplied secondary electrons emitted from the last dynode are finally collected by the anode.
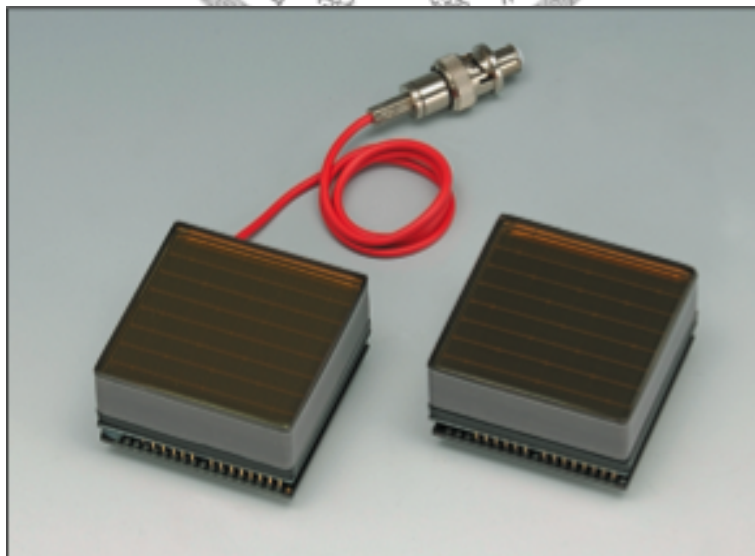
Figure 2.7: Left one is H8500C. [9]

10
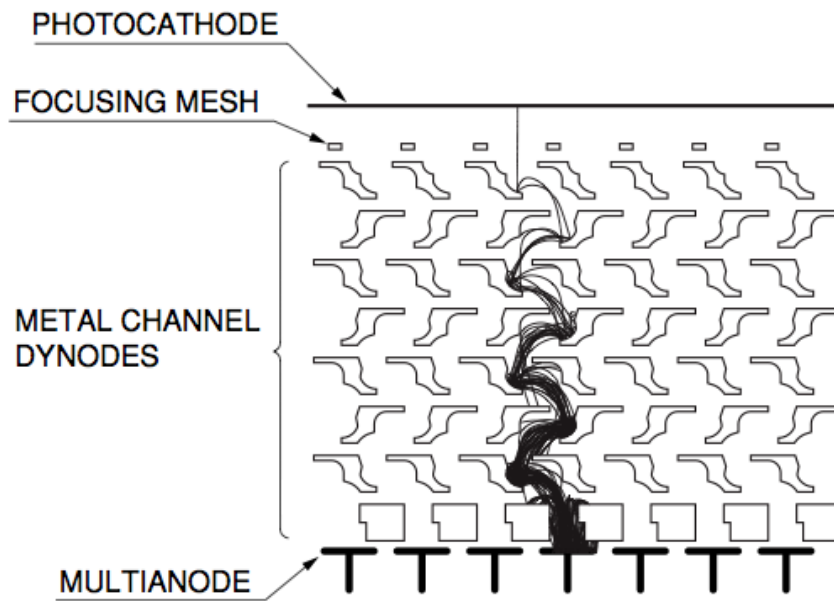
Figure 2.8: Electrode structure and electron trajectories [8]
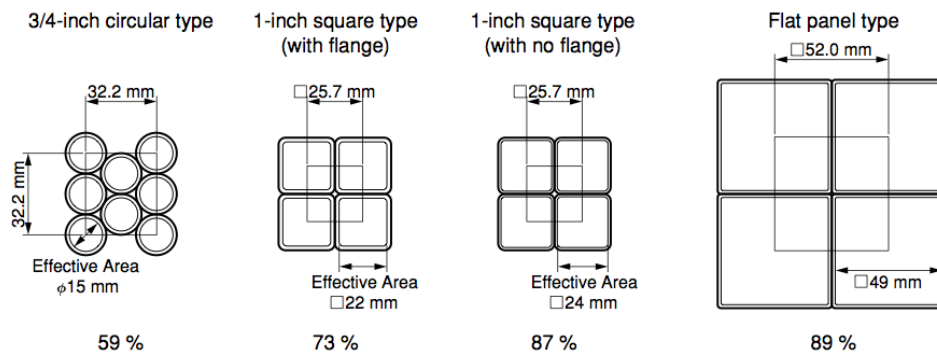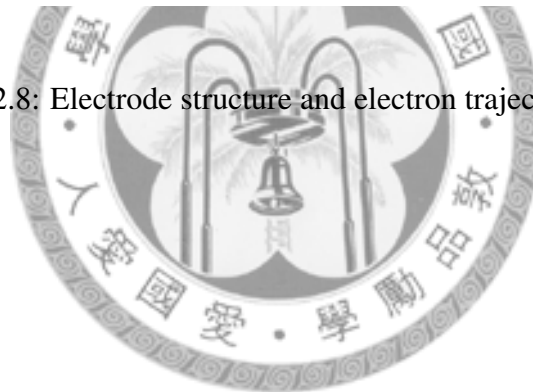
Figure 2.9: Comparison of effective area ratio [8]

The MAPMT we used is Hamamatsu H8500C, which is shown in Figure 2.7. It belongs to metal channel dynode type multianode photomultiplier tubes. Compared to the other types of dynodes, it features very low crosstalk during secondary electron multiplication. Figure 2.8 shows the electrode structure for metal channel dynodes and the associated electron trajectories. Moreover, the window is flat panel type. As shown in Figure 2.9, this kind of MAPMT features a large effective area and minimal dead area (insensitive area). According to data sheet of Hamamatsu [9], size of front window is $52 \times 52mm^2$ and effective area is $49 \times 49mm^2$. So the packing density (effective area / external size) is 89%. In conclusion, this MAPMT has better spatial resolution. Figure 2.10 shows the graphs of typical spectral response and typical gain characteristics. The quantum efficiency between 350 nm and 450 nm is above 20%. The operation voltage is from 700 to 1100 Volt so that the gain is from 10^5 to 3×10^6. Figure 2.11 is an example of anode uniformity. It
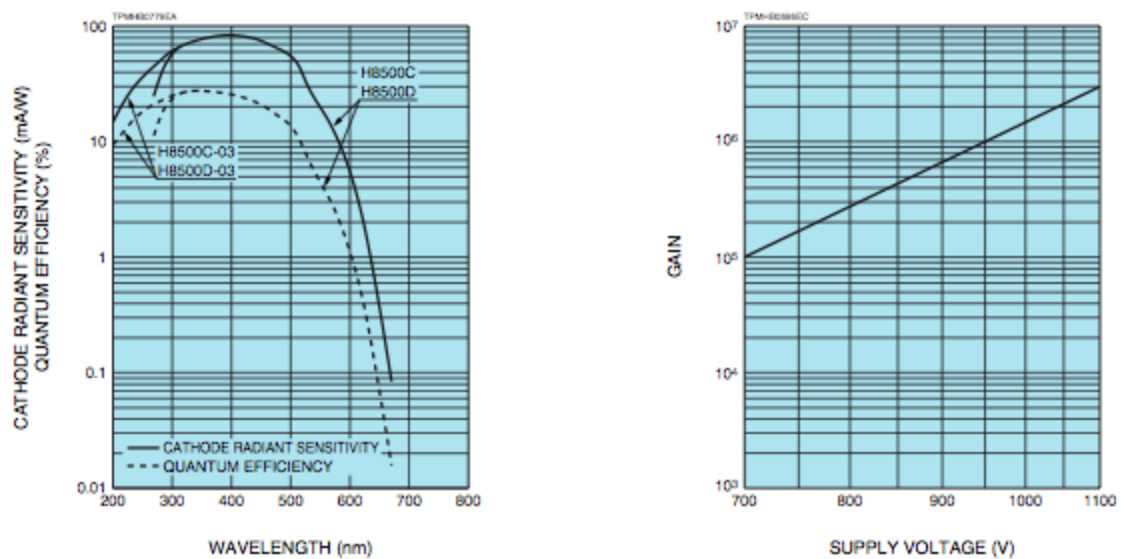
Figure 2.10: Left: Typical Spectral Response, Right:Typical Gain Characteristics [9]

shows different pixels have different gains in one MAPMT. To make uniform gain of each channel, the gain of DCM can be changed by adjusting potentiometer. So the non-uniformity can be minimized. We will talk about it in section 2.3.3.

P1							P8
68	93	88	90	79	71	86	97
83	100	94	95	91	82	89	90
97	98	93	86	82	85	86	82
98	99	87	79	75	81	86	79
95	98	83	71	69	72	77	71
96	94	76	66	65	63	66	61
81	77	62	60	58	54	58	50
75	72	64	62	63	59	65	52

TOP VIEW
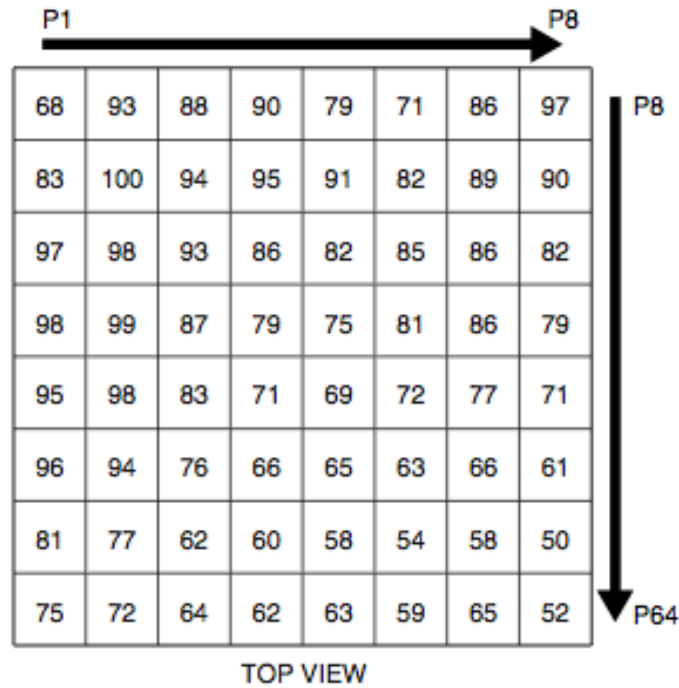
Figure 2.11: Anode Uniformity [9]

2.3.2 Pre-amplifier (Pre-amp)

As mentioned before, anode output charge (current) signal. The Pre-amp convert the input charge signal into differential voltage signal. Figure 2.12 shows the circuit diagram of Pre-amp. The circuit can be divided into two stages: the charge-sensitive stage and differential stage. [10] In first stage, we use IC AD8067 with an RC circuit ($R \sim 170k\Omega$, and $C \sim 1.1pF$). So when a current pulse inputs Pre-amp, the waveform of output signal has a tail with decay time $\sim RC = 170k\Omega \times 1.1pF = 187ns$ and the amplitude $\sim \frac{Q}{C}$ (If the gain of MAPMT is 10^5 and there is a photoelectron produced at photocathode, the amplitude $\approx \frac{1e^- \times 10^5}{1.1pF} \approx 14.6mV$; If the gain of MAPMT is 3×10^6 and there is a photoelectron produced at photocathode, the amplitude $\approx \frac{1e^- \times 3 \times 10^6}{1.1pF} \approx 438mV$). The second stage use Low-voltage differential signaling (LVDS) method to reduce the noise produced in transmission. In this stage, IC AD8131 divides the voltage signal which generated at first stage into two differential voltage signals. The two differential voltage signals, which have same amplitude but opposite polarity, transmits on a pair of wires.
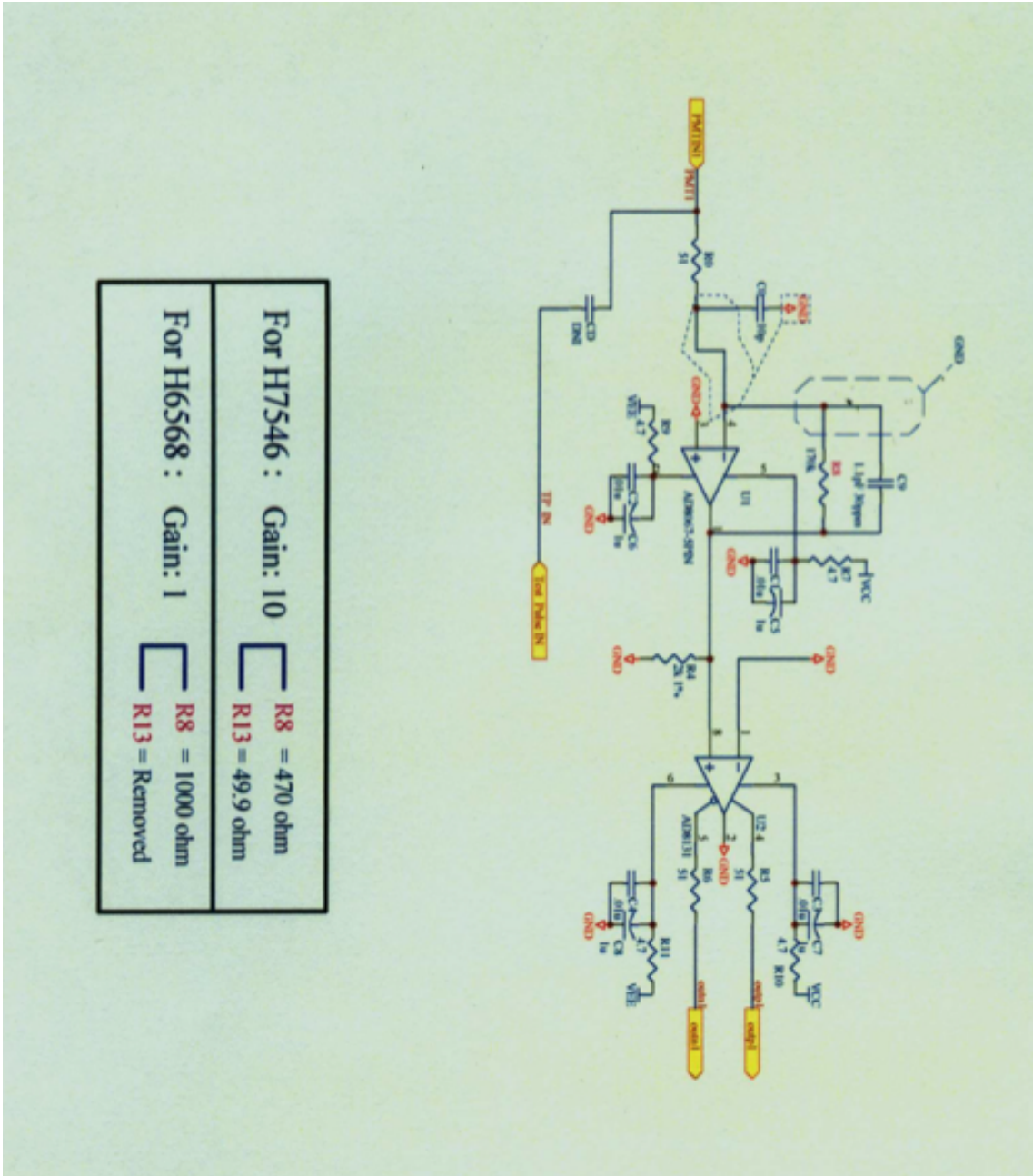
Figure 2.12: schematic of one channel in Pre-amp [10]

14

In transmission, basically, the two signals produce the same background noises. At the receiver, which is DCM, the two signals are compared. Therefore, the background noises are eliminated.
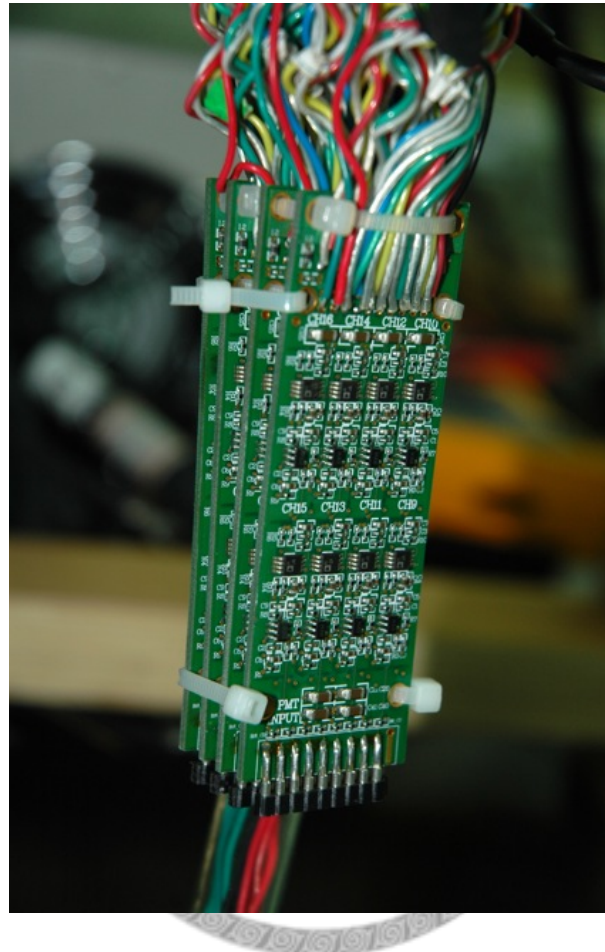
Figure 2.13: Picture of four Pre-amp boards

Figure 2.13 shows a cluster of four pre-amp boards. It provides total 64 channels and fits one MAPMT. There are eight channels and one ground pin on one side of Pre-amp, so totally sixteen channels and two ground pins are on both side.

There are three power lines on a Pre-amp: positive, ground, and negative voltages. Table 2.1 shows the relation between power supply voltages and saturation voltages of Pre-amp. When supply voltage increases, the output dynamic range also increases. For preventing damage IC, we usually choose $\pm 5V$ to drive Pre-amp, and also have a suitable dynamic range ($\sim 3.5V$). To drive one Pre-amp board, current magnitude is about $0.3A$.

Table 2.1: output saturation voltages with supply voltages

Power Supply voltage (V)	±3.0	±3.5	±4.0	±4.5	±5.0	±5.5	±6.0
Saturation voltage (V)	1.76	2.18	2.64	3.08	3.52	3.94	4.34
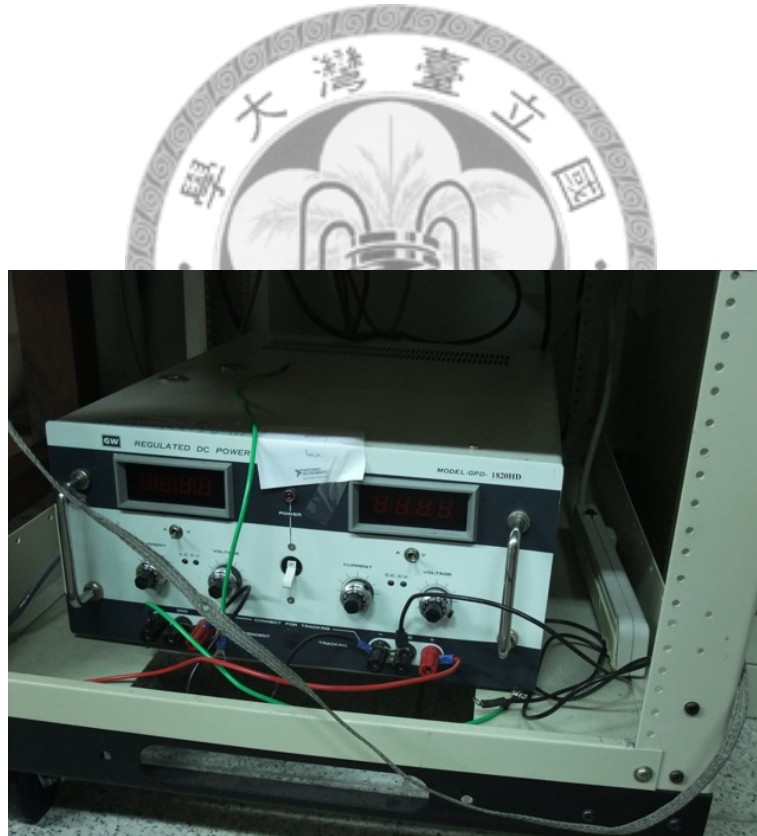
Figure 2.14: Picture of power supply

If we uses several MAPMTs, the current of Pre-amps' power could reach $10A$. Thus, a power supply can load hight current is needed. Figure 2.14 shows the power supply we used to drive Pre-amps.

2.3.3 Data Collection Module (DCM)
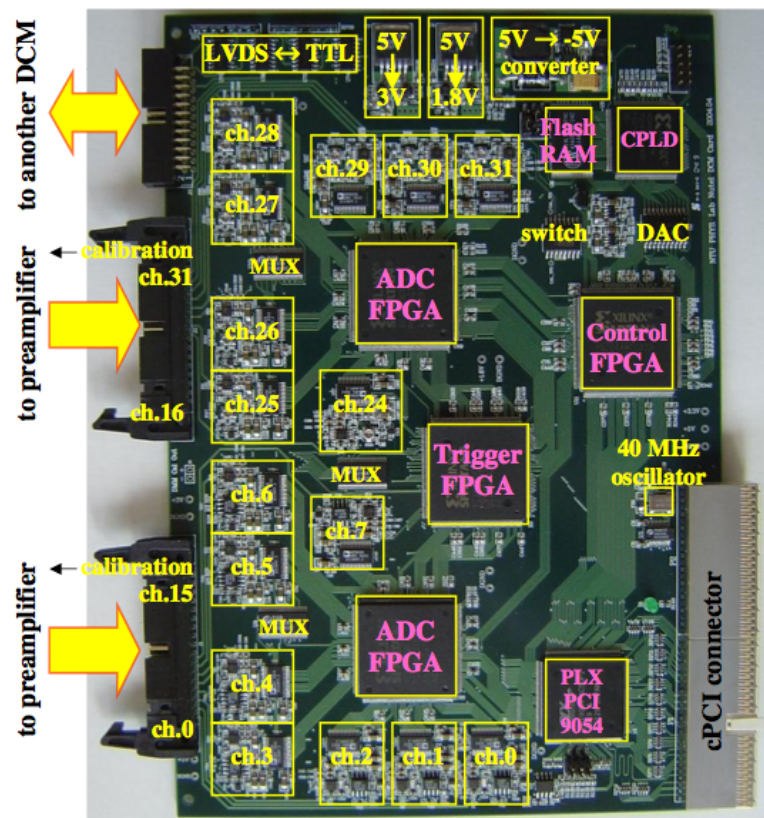
Figure 2.15: Picture of Data Collection Module

Data collection module (DCM) is a cPCI card which receives analog signals from Pre-amps and digitize them every 25 ns. It also does trigger decision and transfers data via cPCI bus. Figure 2.15 shows the photo of DCM. Main parts of hardware design are following:

- 32 analog channels consist of differential receiver amplifier, programmable potentiometer, analog switch for calibration purpose and 40-MHz 10-bit pipelined ADC.

17
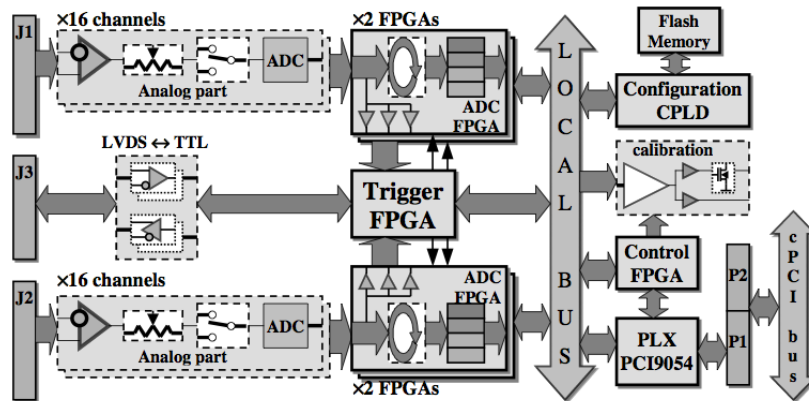
Figure 2.16: Schematics of Data Collection Module

- Four ADC_FPGAs process data from ADCs. Signals for Trigger purpose are calculated inside ADC_FPGA, three programmable discriminators (three different thresholds) at every channel are used for this purpose.

- Trigger_FPGA collects discriminator's outputs from all 32 channels on board and makes a Trigger request according to the logic implemented inside its firmware code.

- LVDS $\Leftrightarrow$ TTL transformers between front panel connector J3 and Trigger_FPGA are used for the connection of Trigger_FPGAs from different DCMs into stand alone system by daisy chain mechanism.

- Flash memory IC is used for the storage data for configurating all FPGAs.

- Configuration_CPLD controls configuration/initialization of all FPGAs using data from the Flash Memory.

- Calibration circuit based on 14-bit DAC is used for the calibration of ADCs and preamplifiers.

- Control_FPGA controls a data transfer process through the local bus, a calibration process and makes a memory (address) distribution for all units inside module.

- PLX PCI9054 is used for connecting the local bus with cPCI bus.

Figure 2.16 shows the schematics of DCM.

Analog part before FPGA

As shown in Figure 2.15, two sockets connect with two Pre-amps (total 32 channels). Before FPGA, differential signals are received with differential receiver amplifier and then programmable potentiometers affect gain of signals. Finally, ADCs convert analog signals into digital signals.
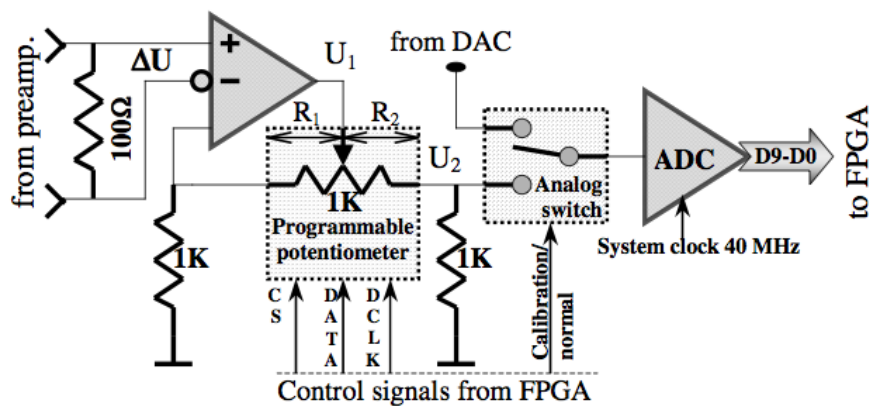
Figure 2.17: Schematics of one channel before FPGA

Figure 2.17 shows the schematics of one channel before FPGA. The main parts of this design are as following:

- Differential receiver amplifier "AD8130A"

- Programmable potentiometer "AD8400-1K"

- Analog switch "NC7SB3157"

- 10-bit 40-MHz pipelined ADC "AD9203RU-28"

As mentioned in Section 2.3.2, output signals after Pre-amp are differential. The differential receiver amplifier compares two signals and output a low-noise voltage signal.

Because gains of pixels in MAPMT are not uniform, there are programmable potentiometers which can adjust gains of channels in DCM. The range of adjusted gain is from $\frac{1}{2}$ to 2. The calculation of gain is as following:

$$U_1 = \Delta U \times \frac{1k + R_1}{1k} \tag{2.1}$$

$$U_2 = U_1 \times \frac{1k}{1k + R_2} \tag{2.2}$$

$$R_1 + R_2 = 1k \tag{2.3}$$

The definition of gain of DCM is

$$G_{DCM} = \frac{U_2}{\Delta U}$$

So from Eq.2.1, 2.2, and 2.3, we found the gain of DCM is depend on resistance R_1.

$$G_{DCM} = \frac{U_2}{\Delta U} = \frac{1k + R_1}{1k + R_2} = \frac{1k + R_1}{2k - R_1} \tag{2.4}$$

As Eq. 2.4, $G_{DCM} = \frac{1}{2}$ if $R_1 = 0$; $G_{DCM} = 2$ if $R_1 = 1k$. In conclusion, the gain of DCM (G_{DCM})can be set from $\frac{1}{2}$ to 2 by adjusting potentiometer to change R_1 value.

The programmable potentiometer is 8-bit so its value is a positive integer from 0 to 255. The R_1 value is determined by

$$R_1 = \frac{P}{255} \times 1k \tag{2.5}$$

Here P is potentiometer value. Thus from Eq. 2.4 and 2.5, we can get the relation between gain and potentiometer. The equation is as following:

$$P = 255 \times \frac{2G_{DCM} - 1}{1 + G_{DCM}} \tag{2.6}$$

According to Eq. 2.6, we can get suitable value of potentiometer to adjust gain we want in DCM. Actually, the total gain in one channel is contribution of MAPMT, Pre-amp, and DCM.

$$G_{total} = G_{MAPMT} \times G_{preamp} \times G_{DCM} \tag{2.7}$$

20

As a result the non-uniform gains of MAPMT and Pre-amps can be eliminated by programmable potentiometers if the ratio of maximum gain and minimum gain isn't larger than 4:1.

Analog switch is used for calibration ADC (pedestal and gain), it could switch ADC input between signal from receiver and signal from 12-bit DAC. ADC digitizes data in 10-bit 40MHz (every 25 ns). Dynamic range of ADC is 2 V, that means $\sim 2\frac{mV}{bin}$. The digitized data from ADC pass to four FPGAs called ADC_FPGA.

ADC_FPGA
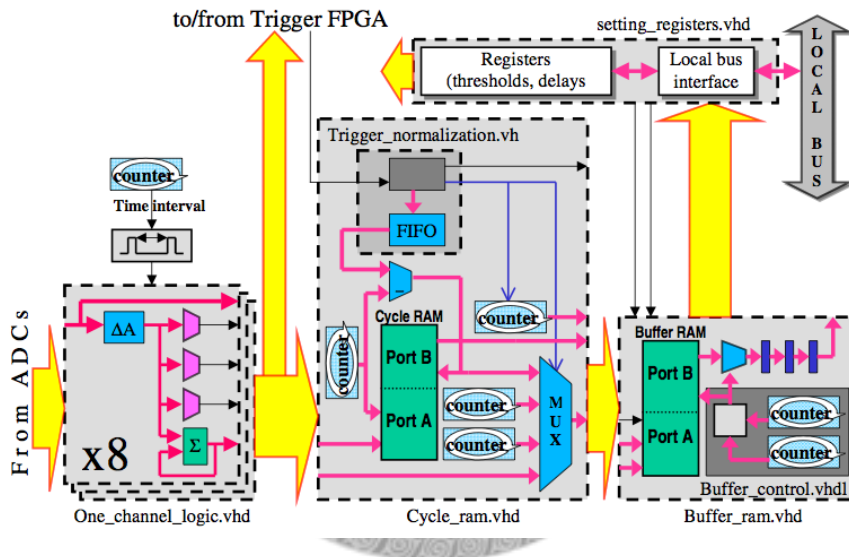
Figure 2.18: Schematics of ADC_FPGA Module

ADC_FPGA consisted of comparators, Cycle RAM, and Buffer RAM. There are four ADC_FPGA in one DCM. Thus, one ADC_FPGA deals with eight channels. Schematics of ADC_FPGA is shown in Figure 2.18. In one channel, data from ADC pass to comparators. A charge is calculated as $\Delta A = A_{i+1} - e^{-\frac{25}{187}} \times A_i \approx A_{i+1} - \frac{7}{8} \times A_i$. Here 187 (ns) means decay time constant of Pre-amp and 25 (ns) means one system clock. This value compares with three programmable thresholds (VHL, HL, LL). Figure 2.19 shows the idea of calculating input charge. Outputs from the comparators pass to the Trigger FPGA for making a Trigger decision and are delayed inside Cycle RAM together with the ADC

21
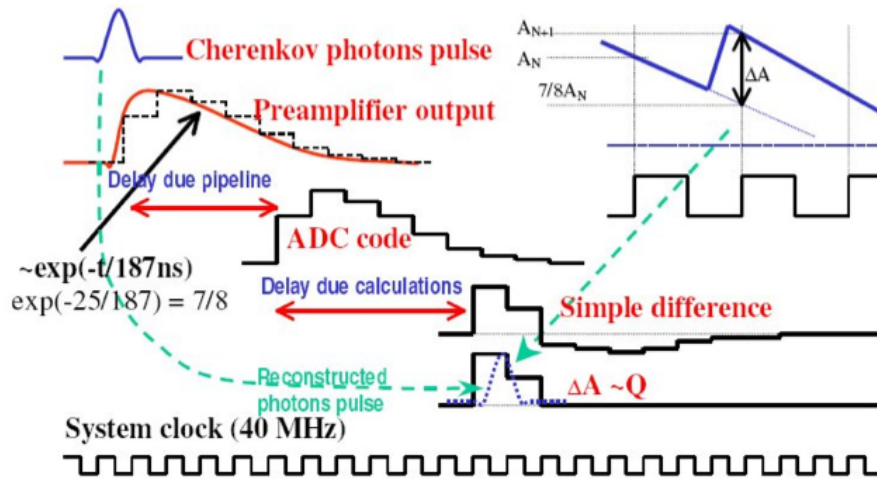
Figure 2.19: Schematics of calculating charge every clock

data on a time needed for the Trigger operation. A size of Cycle RAM is 256×96-bit words. Format of the data inside Cycle RAM is 12 bits per clock every channel. Here 10 bits are ADC code and 2 bits are comparators output. Thus, it allows to make a maximal delay of $256 \times 25ns = 6.4\mu s$ for the Trigger decision.

After receiving trigger signal from Trigger_FPGA, the triggered event will stored into Buffer RAM. Used delay (also from Trigger_FPGA), it will trace back n-th (1-256th) clock data before in Cycle RAM. Size of a Buffer RAM is 256×128-bit. One event size in Buffer RAM is 8×128-bit, so Buffer RAM can store 32 events. To maximize data transfer rate, the data are sent to single board computer (SBC) when every 16 events are filled in Buffer RAM. Figure 2.20 shows data formats in Cycle RAM, Buffer RAM, and CPCI bus respectively.

Trigger Decision

Trigger_FPGA receive VHL, HL, and LL hits from 4 ADC_FPGAs. It will make a trigger decision with these three hits, and also receives trigger request from left DCM. This incoming trigger request will do OR logic operation with the trigger decision, then pass result to trigger daisy-chain sending to right DCM. Master DCM (rightmost DCM) will

22
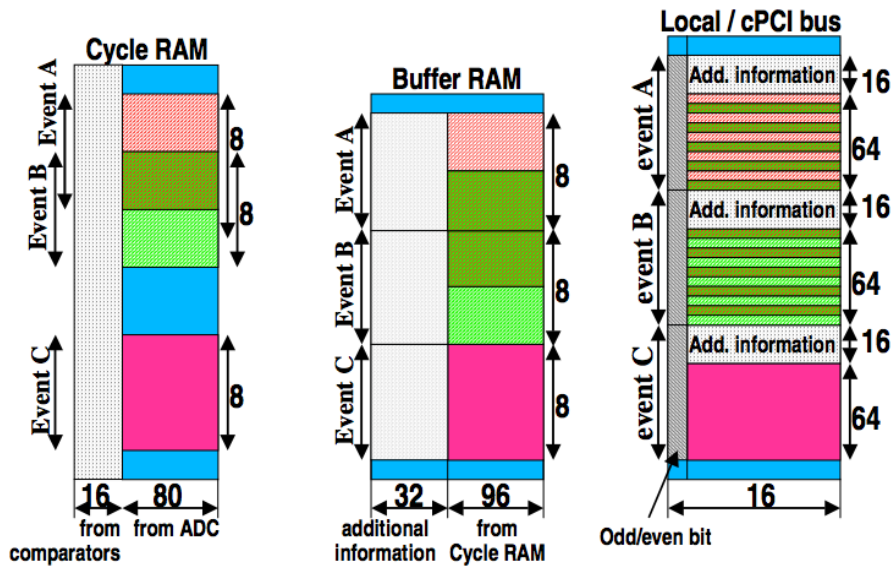
Figure 2.20: Data formats in Cycle RAM, Buffer RAM, and CPCI bus.

make a final trigger decision, and pass trigger signal to its ADC_FPGA and other Slave DCMs.

Data Fomat

A data format on the local and cPCI buses is shown in Figure 2.21. Because of the 32-bit cPCI is used, two FPGAs are read at the same time: channels 0-7 (16-23) via D0-D15, channels 8-15 (24-31) via D16-D31. To check correct data transmission the D15 (D31) bit is used as odd/even bit for D0-D14 (D16-D30). One event is of 80×2 words for 32 channels. To reduce a dead time due interrupt latency in cPCI a block from 16 events is read at once, a size of this block is $160 \times 16 = 2560$ 32-bit words for one DCM (32 channels).

2.3.4 Data Acquisition (DAQ)

The DAQ system of NuTel includes the chassises, each with one SBC (single board computer) and 16 DCM (Data Collection Modules). We choose CompactPCI (CPCI) as our bus standard for hardware form and data transmission between devices. The

#	D15 D31	D14 D30	D13 D29	D12 D28	D11 D27	D10 D26	D9 D25	D8 D24	D7 D23	D6 D22	D5 D21	D4 D20	D3 D19	D2 D18	D1 D17	D0 D16
1	0	1	0	1	0	1	0	1	0	1	0	1	0	1	0	1
2	0/1	Trigger [14:0]														
3	0/1	Trigger [29:15]														
4	0/1	Time [14:0]														
5	0/1	Time [29:15]														
6	0/1	Time [44:30]														
7	0/1	0	0	0	0	0	0	0	Used Delay [7:0]							
8	0/1	0	FPGA number [5:0]						Cycle RAM address [7:0]							
9	0/1	Integrated background charge [14:0] channel # 0														
16	0/1	Integrated background charge [14:0] channel # 7														
17	0/1	0	0	VHL	HL	LL	ADC code [9:0] channel # 0, time slot # 0									
24	0/1	0	0	VHL	HL	LL	ADC code [9:0] channel # 0, time slot # 7									
25	0/1	0	0	VHL	HL	LL	ADC code [9:0] channel # 1, time slot # 0									
80	0/1	0	0	VHL	HL	LL	ADC code [9:0] channel # 7, time slot # 7									

Figure 2.21: Data format on the cPCI bus

PCI(Peripheral Component Interconnect) standard is developed by Intel circa 1990. The PCI architecture was designed to replace ISA architecture as dominant choice of bus standard in PC market. Compact PCI system is Eurocard-based PCI boards which are connected via passive PCI backplane. According to the height of Eurocard, there are two kinds of popular size: 3U, and 6U. In DCMs, IC PCI 9054 is used as communicating with DCM via CPCI bus. For our 32-bit width PCI, it runs at 33.33 MHz, its burst transfer rate can reach 133 MB per second (33.33 MHz $\times$ 32 bits/8 bits=133 MB/s), while in local bus, system clock runs at 40 MHz. PCI 9054 could manage transfers of data between local bus of DCM (40 MHz) and PCI bus(33.33 MHz).

2.4 Analysis Software

Figure 2.21 shows the data format of a raw data file. According to it, we can get event data (ADC, time, trigger, etc.) from binary file. We use Python language to develop our analysis software. The operation speed of Python is slower than that of C++, but it has

advantages of easy reading, and easy writing. Thus, using it reduce a lot of development time. In this thesis, graphs, histograms, and fitting patterns are mostly drawn with ROOT which is a framework for data processing, born at CERN, at the heart of the research on high-energy physics.

Chapter 3

Charge Signal Reconstruction

3.1 Introduction

As mentioned in previous chapter, a charge pulse from MAPMT is converted to a differential voltage signal through Pre-amp. Furthermore, DCM converts this signal into 8 ADC numbers. However, the issue that how to get original signal from ADC counts is the most important before any measurement. Thus, this chapter mentioned the way we reconstruct signal from digital data.

First, we measured the decay time constant of Pre-amp for each channel. Then, the decay shape of waveform after Pre-amp should be known. Thus, we could use it to reconstruct charge signal.

3.2 Time Constant Measurement

As mentioned in Section 2.3.2, the preamp was made by RC circuits, and the default decay time is $\tau_2 = R_8 C_9 = 170k\Omega \times 1.1pF = 187ns$. Actually, the values of resistances and capacitances are different slightly for different channels. Before reconstructing charge signal, we should know the actual decay time in each channel firstly. Thus, to measure
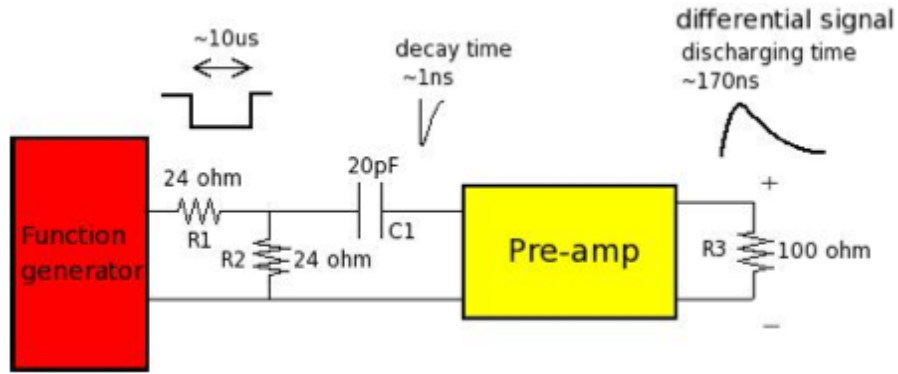
Figure 3.1: Schematics of calibration circuit for Pre-amp. Function generator send a negative square pulses, then capacitor is charged at falling edge. Thus, a current pulse, whose decay time is less than 1 ns, is sent into Pre-amp. [10]

real decay time is needed. At first, a pulse signal is produced by a function generator and a circuit. Figure 3.1 shows the schematic we used to simulate MAPMT's charge signal.

The simulated charge signals had sent to preamp channel by channel. Figure 3.2 shows the waveform of signal after Pre-amp. To get the decay time constant, we adopted two kinds of fitting methods. [10]

As shown in Figure 3.3, the waveform is divided into four regions. The four regions are pedestal region, rising region, turning region, and decay region. The fitting equation we use to fit waveform is as follows:

$$
V = \begin{cases}
y_0 & \text{if } t < T_1, \\
y_0 + A_1(1 - e^{-(\frac{t-T_1}{\tau_1})}) & \text{if } T_1 \leq t < T_2, \\
y_1 + \alpha(t - T_2) + \beta(t - T_2)^2 & \text{if } T_2 \leq t < T_3, \\
y_0 + A_2 e^{-(\frac{t-T_3}{\tau_2})} & \text{otherwise.}
\end{cases}
\tag{3.1}
$$

Figure 3.3 also shows the fitting result, and the rising time constant τ_1 and the decay time constant τ_2 have been calculated. As a result, time constants of all channels were measured, and they were recorded in database.
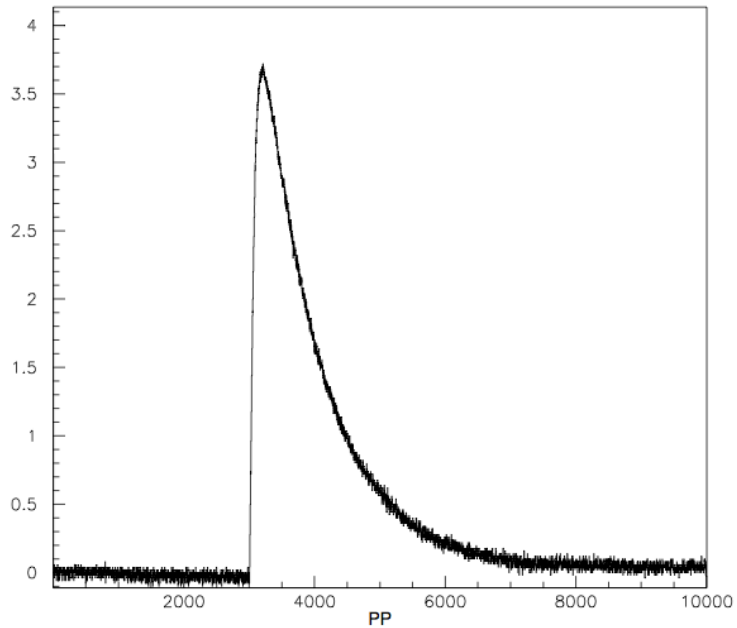
Figure 3.2: The waveform of output signal after Pre-amp
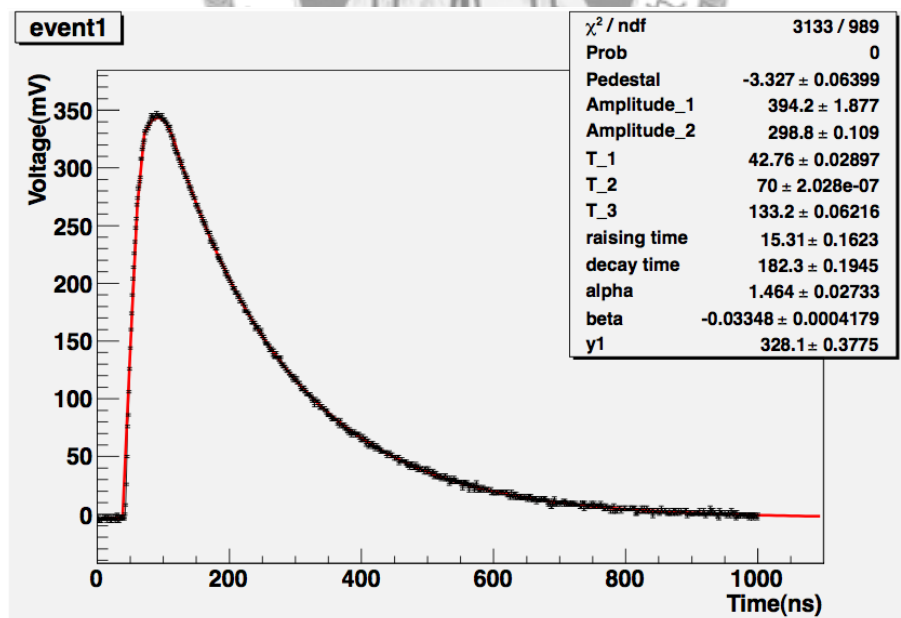
Figure 3.3: The waveform is divided into four regions to fit. (Pre-amp 15, ch0) It is called divide-fit.
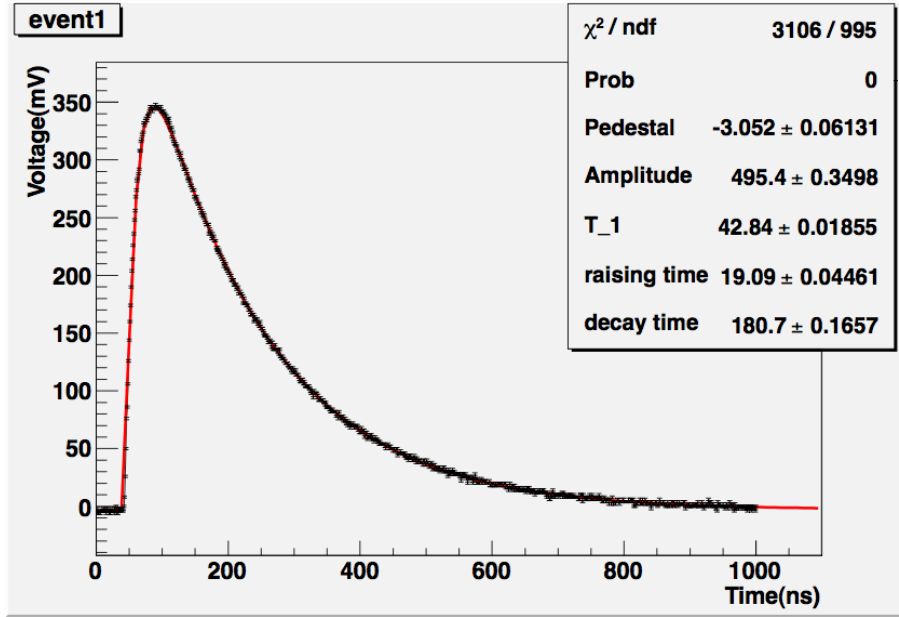
Figure 3.4: The waveform is using one function to fit. (Pre-amp 15, ch0) It is called merge-fit.

Figure 3.4 shows another fitting method. The fitting equation is as following:

$$V = \begin{cases} y_0 & \text{if } t < T_1, \\ y_0 + A_1(1 - e^{-(\frac{t-T_1}{\tau_1})})e^{-(\frac{t-T_1}{\tau_2})} & \text{otherwise} \end{cases} \tag{3.2}$$

It only uses one function to fit rising, turning, and decay regions. It merges rising function with decay function. The reason is that voltage signal also decays when it rises. We can expect that the rising time constant from merge-fit is larger than the one from divide-fit. Comparing Figures 3.3 and 3.4, the rising time constant from merge-fit is really bigger. But the most important term is decay time constant because it concerns signal reconstruction. The fitting decay time constants from two method are close and the difference is about 1%. They are recorded in a database file and we can use them to reconstruct signal.

3.3 Reconstruction

Figure 3.5 shows the graph of ADC values to time. There are eight ADC values in one event. The interval between ADCs is 25 ns (1 clock). As Section 2.3.3 mentioned, input
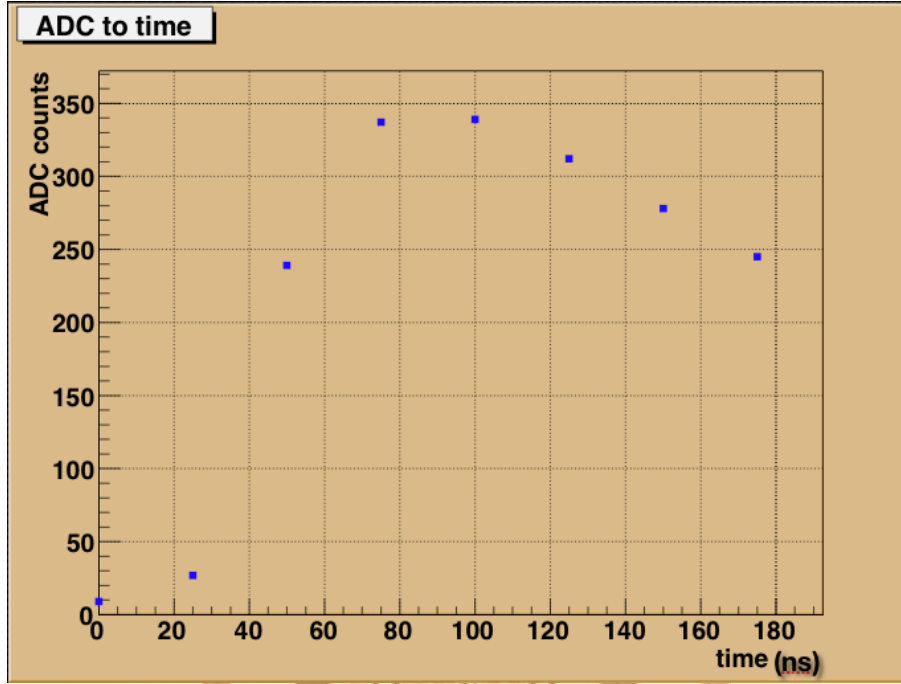
Figure 3.5: The graph of per event in one channel. X-axis means time and Y-axis means ADC value. One clock is 25 ns.

charge is calculated as $\Delta A = A_{i+1} - e^{-\frac{187}{25}} \times A_i$. Thus, the total input charge within 200 ns can be reconstructed by following formula:

$$\sum_{i=1}^{7} \Delta A = \sum_{i=1}^{7} (A_{i+1} - e^{-\frac{25}{\tau_2}} A_i) \tag{3.3}$$

where A_i represents pedestal-subtracted ADC, and τ_2 means decay time constant.

3.4 Result and Conclusion

As Section 3.2 mentioned, we can use function generator and circuit to simulate a MAPMT signal to send to Pre-amp. Then, we use DAQ to take data and read raw file. Figure 3.6

31

shows the histogram of reconstructed charges. It shows the rms of reconstructed charge is about 3 mV. As mentioned in Section 2.3.2, the pulse height of single photoelectron is from 14.6 mV to 438 mV when load voltage is from 700 V to 1100 V. For most data, we would like to adjust voltage, which supplies MAPMT, to make signal around one or two thousands. So the bias made in reconstruction is small in comparison with signal.
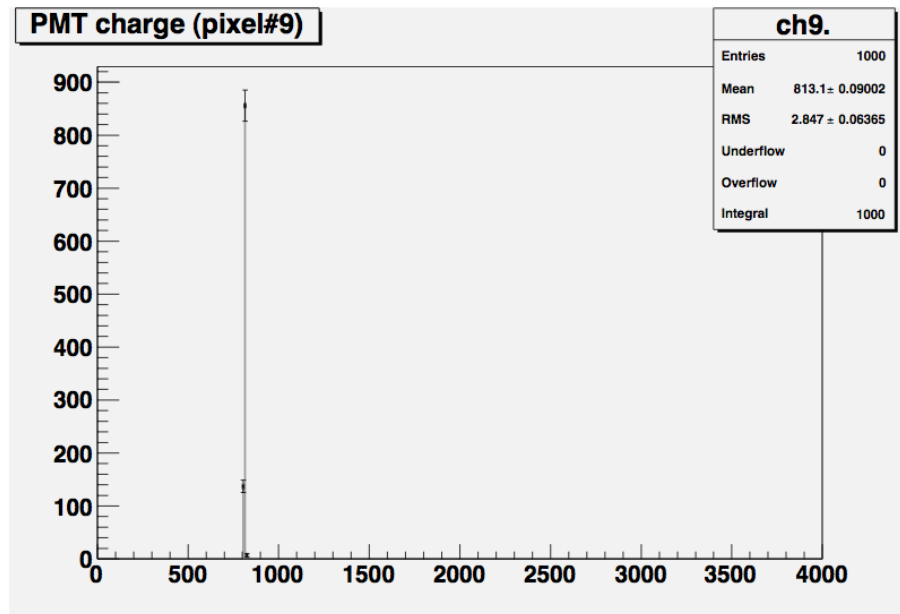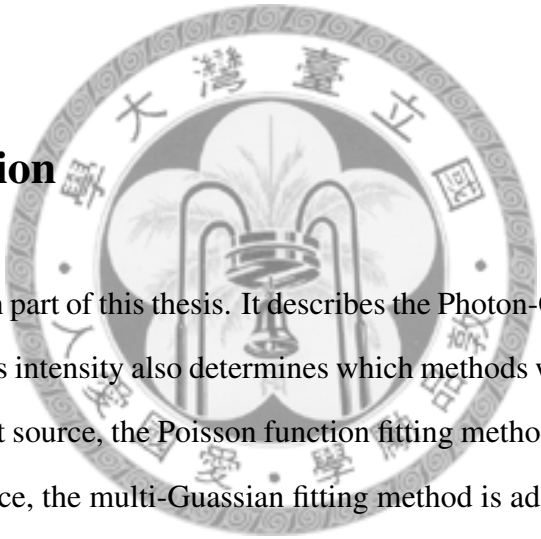
Figure 3.6: The histogram of reconstructed charges with the same 1000 input signals (Pre-amp 15, ch9). The unit of X-axis is mV.

Chapter 4

Photon-Counting

4.1 Introduction

This chapter is the main part of this thesis. It describes the Photon-Counting Methods with MAPMT. The luminous intensity also determines which methods we adopted. For normal luminous intensity light source, the Poisson function fitting method is adopted. For single photon order light source, the multi-Guassian fitting method is adopted. Finally, we used HPD to confirm the measurement result with MAPMT.

4.2 Set-up

Because MAPMT has very good luminous sensitivity, even few photons can be detected. The good black box for the light source and MAPMT are needed. The light source which we adopted is light-emitting diode (LED). We did some test for the uniformity of the LED light.

4.2.1 Black Box

The black box was made by aluminum. Its size is $180cm \times 25cm \times 26.5cm$. Inside box, there are black cloths on the surface to reduce the reflection of light. On one side of the box, there is a LEMO connector which we use to send signals into box. On the other side, there is a circle hole. Its diameter is $8.5cm$. A black plastic tube is through the hole, and we use it to put our signal cables. We put some black cloths in the entrance of tube so that the light is hard to enter.The tube is curved and long so that the few entering light is hard to affect our experiment.

4.2.2 Light Source—LED

Because MAPMT is sensitive with light, the LED is used to be the light source. In NuTel project, the wavelength of the light that we want to observe is from 350 nm to 450 nm, so the purple LED (Figure 4.1), whose wavelength is about 400nm, is be adopted to calibrate electronic readout system. The function generator could control light source by sending square pulses to LED. The light intensity, frequency and width of light could be adjusted through function generator.

Another issue is how uniform the purple LED is. Figure 4.2 shows the brightness of LED on different angle isn't uniform. The MAPMT we used has 64 channels. The dynamic range of received signal is determined on operating voltage, so it could not change the dynamic range of channels respectively. If the LED light distribution is not very uniform, the signals in different channels would fluctuate a lot. So we couldn't get good signal resolution.

We used an avalanche photodiode (APD) to measure the uniformity of LED light. An APD is a highly sensitive semiconductor electronic device that exploits the photoelectric effect to convert light to charge. The APD was put at the position which is 140 cm away from LED. We used the multimeter to measure the output current which represents light intensity. The APD was fixed on a movable frame, so the APD could move in
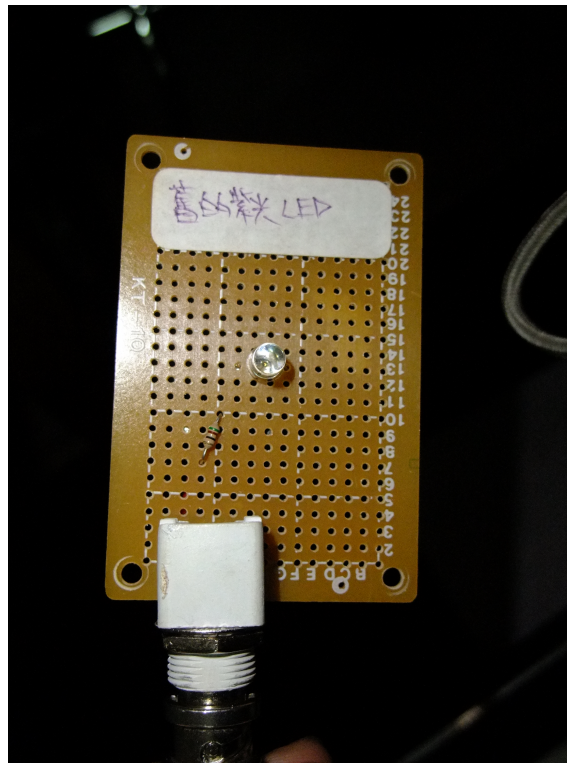
Figure 4.1: The purple LED
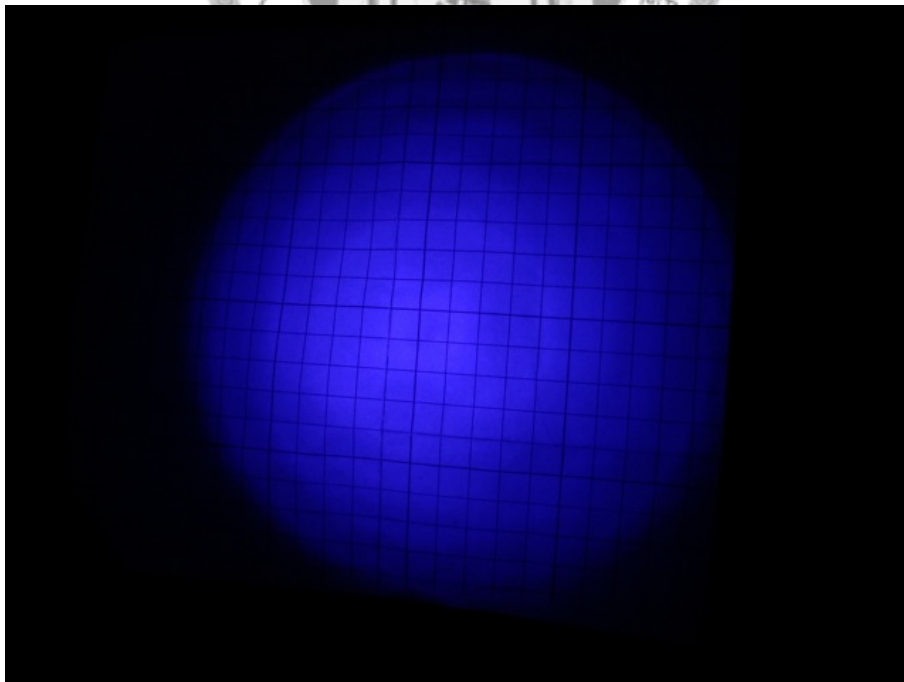
Figure 4.2: The uniformity of LED

$13cm \times 13cm$ area. Figure 4.4 shows the brightness distribution of LED in $13cm \times 13cm$
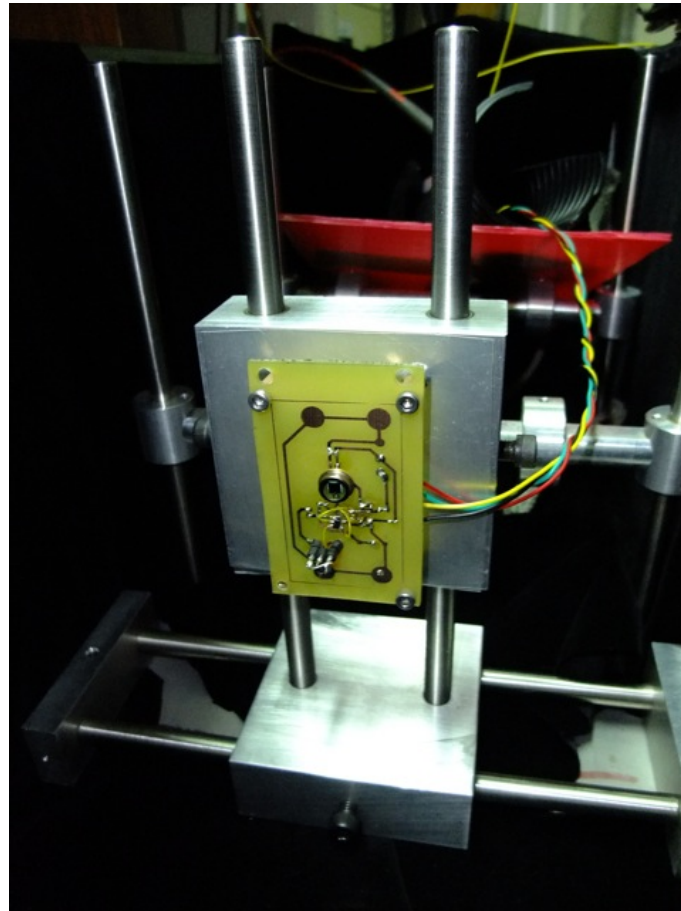
Figure 4.3: Avalanche photodiode and movable frame

area. The areas of MAPMT we used are $2cm \times 2cm$ and $5cm \times 5cm$. In center $2cm \times 2cm$ region, the fluctuation of brightness is less than 5%. In center $5cm \times 5cm$ region, the fluctuation of brightness is less than 10%. As a result, the light source have only 10% difference in different channels. However, there is 10-bit resolution in our electronics. Therefore, different light intensities in channels doesn't affect our experiment.

4.2.3 External Trigger

In our design, we have two kinds of trigger methods. The first method called self-trigger. We set threshold numbers for different channels, and the event is recorded when input signal exceeds threshold value. It is used in observation. For the purpose of calibration,
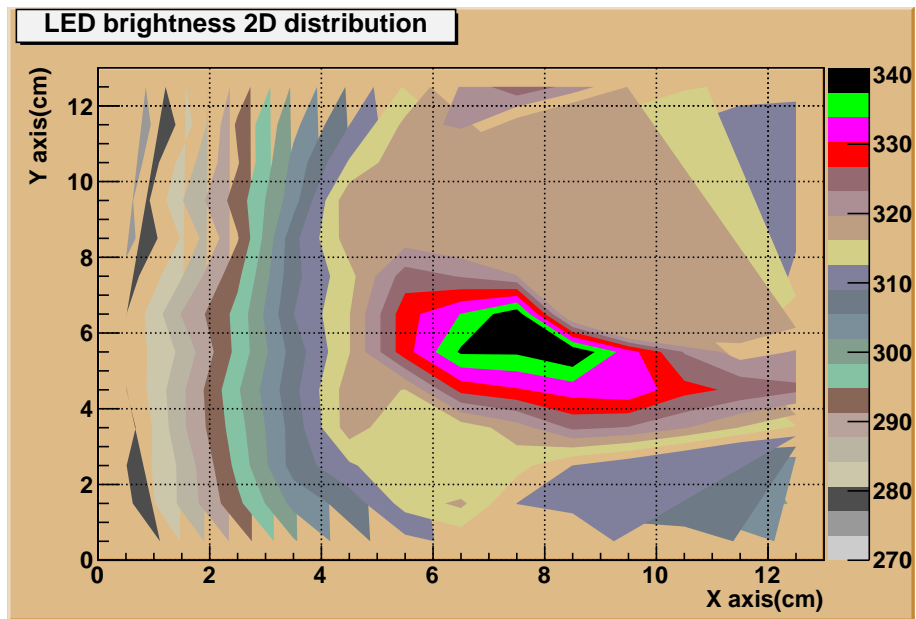
Figure 4.4: The brightness distribution of LED

Figure 4.5: Function Generator drives LED and sends a TTL trigger signal to DAQ

we used external trigger to get the signal we can control. Figure 4.5 shows a function generator which sends pulses to drive LED and TTL trigger to DCM. The trigger events are determined by function generator, and therefore the LED signals are recorded.

4.3   Pulse Height Spectrum

As Section 4.2 mentioned, we used a function generator to drive LED and used external trigger to take data. The events are triggered only when LED shines, so external trigger gets rid of dark current events. Figure 4.6 shows the reconstructed pulse height spectrum. The distribution depends on light intensities and gain. Different light sources or different high voltage drove MAPMT determine the distributions. In following two sections, we will mention how we get gain and light intensities from these data.

4.4   Method

To count photoelectrons, knowing what distributions of pulse height spectrum is important. So in this section, we first discuss three distributions: the Binomial, Poisson, and Gaussian distributions. In different light intensity level, we use different functions to fit the spectra.

4.4.1   Distributions

Binomial

The binomial distribution applies to situations where we conduct a fixed number N of independent trials, each of which has only two possible outcomes – success (with probability p) or failure (with probability $1 - p$). Then the probability of obtaining r successes is given by

$$P(r) = \frac{N!}{r!(N-r)!}p^r(1-p)^{N-r} \tag{4.1}$$
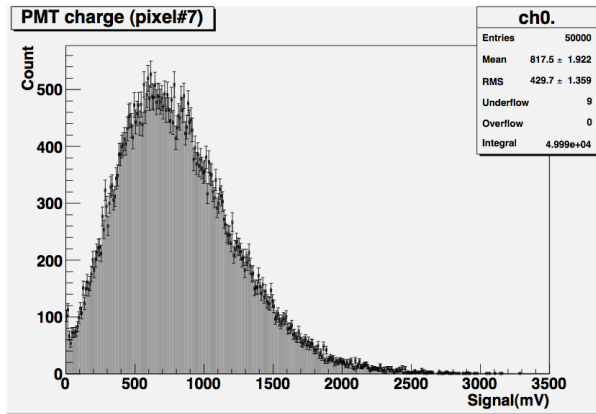
(a) HV -850V and LED 4.7V-height & 10ns-width
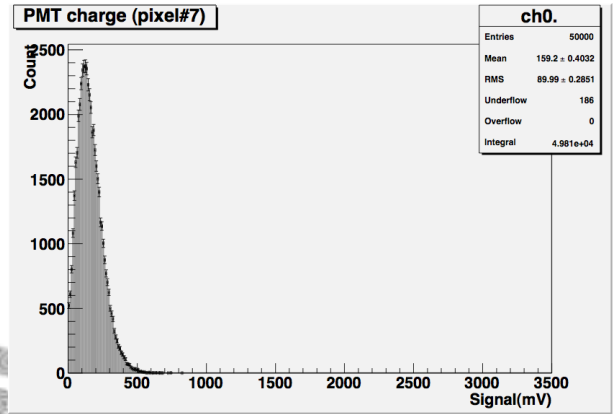
(b) HV -720V and LED 4.7V-height & 10ns-width
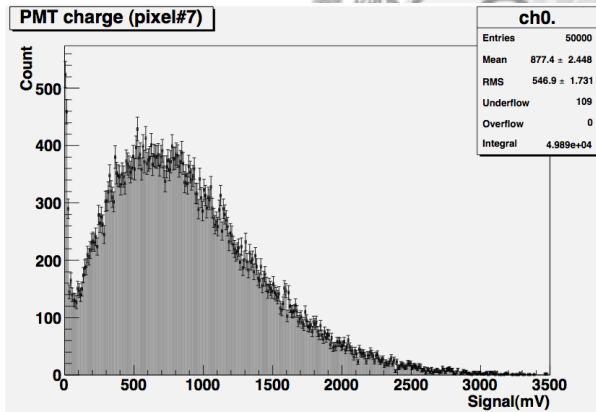
(c) HV -900V and LED 4.4V-height & 10ns-width
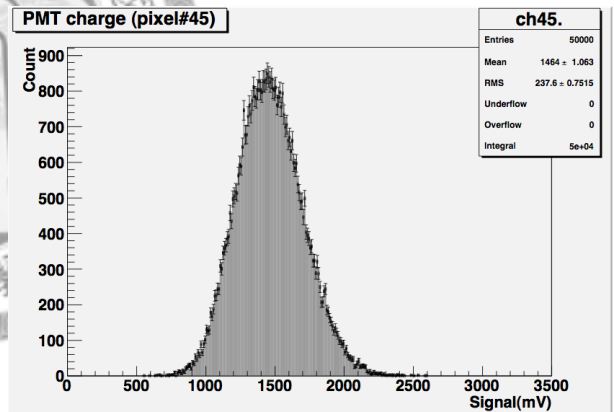
(d) HV -700V and LED 5V-height & 26ns-width

Figure 4.6: The reconstructed pulse height spectrum of measuring different light intensities with MAPMT H8500C GA1824 on different HV.

for values of r from 0 to N. [11]

The expectation value of the number of successes r is

$$\bar{r} = \sum r P(r) = Np. \tag{4.2}$$

The variance of the distribution is given by

$$\sigma^2 = Np(1-p). \tag{4.3}$$

We see from Eqs. 4.1 and 4.2 that

$$\sigma^2 \leq \bar{r}, \tag{4.4}$$

where the equality holds only for $p = 0$.

Poisson

This is the limit of the binomial distribution as
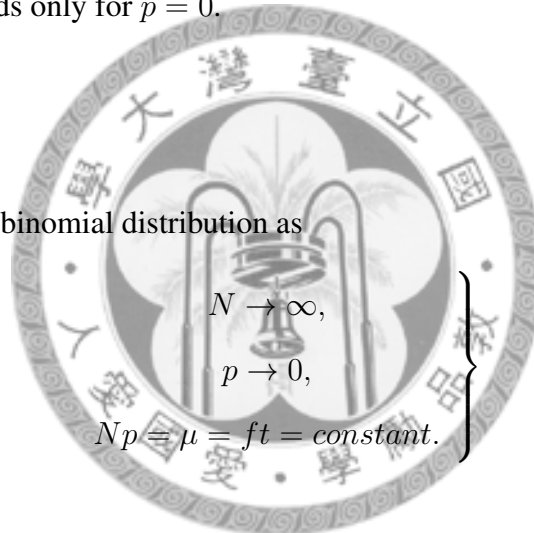
$$\left.\begin{aligned} N &\to \infty, \\ p &\to 0, \\ Np = \mu &= ft = constant. \end{aligned}\right\} \tag{4.5}$$

Then

$$\begin{aligned} P_\mu(r) &= \frac{(ft)^r}{r!} e^{-ft} \\ &= \frac{\mu^r}{r!} e^{-\mu} \\ &= \frac{Np^r}{r!} e^{-(Np)} \end{aligned} \tag{4.6}$$

This is the probability of observing r independent events in a time interval t, when the counting rate is f the expected number of events is μ. And from eq. 4.4, the variance is also μ. Thus, the standard deviation σ is as

$$\sigma = \sqrt{\mu}. \tag{4.7}$$

[11]

Gaussian

This is the limit of the binomial distribution as

$$\left.\begin{array}{l} N \to \infty \\ 0 < p < 1 \end{array}\right\}. \tag{4.8}$$

Then the binomial distribution becomes Gaussian distribution as

$$P(x) = \frac{1}{\sqrt{(2\pi)}\sigma} exp\left(-\frac{(x-\mu)^2}{2\sigma^2}\right), \tag{4.9}$$

This is the probability of observing x independent events, when the expected number of events is μ and standard deviation σ [11]. And the expected number and standard deviation is given by

$$\mu = Np, \sigma^2 = Np(1-p). \tag{4.10}$$

Unlike binomial and Poisson distributions, the Gaussian is a continuous function.

4.4.2 Statistics in MAPMT

As mentioned in Section 2.3.1, in a MAPMT there are two main stages determining signal distribution. First one is photoelectric effect at photocathode, and the other one is secondary electron emission at dynodes.

Photoelectric Effect

In first stage, we assume that N photons hit on photocathode and the quantum efficiency of photocathode is p, thus each photon have probability p to become one photoelectron and probability $1-p$ to disappear. This kind of condition fits the Binomial distribution [12], so the probability distribution in first stage will follow Eq. 4.1. But the number of photons LED emitted should not be constant, and it should obey Poisson distribution. [13] [12] Hence $P_1(x; N)$ is the probability that x photons will arrive when N is the average number photons arriving:

$$P_1(x; N) = \frac{N^x}{x!}e^{-N}. \tag{4.11}$$

So the probability of exactly x photons falling on the photocathode and producing n photoelectrons is as following:

$$P_2(n; x, p, N) = P_1(x; N)\frac{x!}{n!(x-n)!}p^n(1-p)^{x-n}, \qquad (4.12)$$

The probability that n photoelectrons will be produced when an average of N photons fall on the photocathode is $P_3(n; p, N)$ and it is just the sum of $P_2(n; x, p, N)$ over all allowed values of x. The allowed values of x run from n to infinity.

$$
\begin{aligned}
P_3(n; p, N) &= \sum_{x=n}^{\infty} P_2(n; x, p, N) \\
&= \sum_{x=n}^{\infty} \frac{N^x}{x!}e^{-N}\frac{x!}{n!(x-n)!}p^n(1-p)^{x-n}
\end{aligned}
\qquad (4.13)
$$

Replacing $(x-n)$ with j, we get

$$
\begin{aligned}
P_3(n; p, N) &= \frac{e^{-N}}{n!}p^n\sum_{x=n}^{\infty}\frac{N^x}{x!}\frac{x!}{(x-n)!}(1-p)^{x-n} \\
&= \frac{e^{-N}}{n!}p^n\sum_{j=0}^{\infty}\frac{N^jN^n}{j!}(1-p)^j \\
&= \frac{e^{-N}}{n!}(Np)^n\sum_{j=0}^{\infty}\frac{(N-Np)^j}{j!} \\
&= \frac{e^{-N}}{n!}(Np)^ne^{(N-Np)} \\
&= \frac{(Np)^n}{n!}e^{-(Np)} \\
&= \frac{(\mu)^n}{n!}e^{-\mu},
\end{aligned}
\qquad (4.14)
$$

where μ means average photoelectrons [13]. Comparing Eq. 4.14 with Eq. 4.5, we see that the distribution of photoelectrons is Poisson and its mean value equals to the product of the quantum efficiency of photocathode and the average number of incident photons.

Dynodes Processes

In the second stage, each dynode amplifies electrons several times. For our MAPMT, there are twelve dynodes and gain is about $10^5 - 10^7$ so the mean of electrons after anode is very large. Therefore, the response of a multiplicative dynode system to a single

photoelectron can be approximated by a Gaussian distribution. It had be derived by R. Foord, R. Jones, C. J. Oliver, and E. R. Pike in Reference [14]. Each secondary emission process has generally been assumed to follow Poisson statistics and g is the mean gain per stage. For a large number of stages, the pulse height distribution should be gaussian when $g \gg 1$, and Poisson when $g \ll 1$. Therefore, the pulse height distribution for a single photoelectron input can be expressed as

$$G_1(x) = \frac{1}{\sigma_1 \sqrt{2\pi}} exp\left(-\frac{(x-g)^2}{2\sigma_1^2}\right), \qquad (4.15)$$

where x is the variable charge, g is the gain of MAPMT, and σ_1 is the corresponding standard deviation of the charge distribution. When the process is initiated by n photo-electrons, the pulse height distribution is a convolution of n one-electron cases:

$$G_n(x) = \frac{1}{\sigma_1 \sqrt{2\pi n}} exp\left(-\frac{(x-ng)^2}{2n\sigma_1^2}\right). \qquad (4.16)$$

[12] Note that this distribution has the correct limit for $n \to 0$:

$$G(x) = \delta(x),$$

where $\delta(x)$ is the delta function . This condition ensures that the amplification of an input zero charge results in zero charge at the output.

The response of an ideal noiseless PMT can now be readily found. In this case the resulting output signal is simply a convolution of the distributions Eq.4.14 and Eq.4.16:

$$\begin{aligned}
S_{ideal}(x) &= P_3(n; \mu) \otimes G_n(x) \\
&= \sum_{n=0}^{\infty} \frac{\mu^n e^{-\mu}}{n!} \frac{1}{\sigma_1 \sqrt{2\pi n}} exp\left(-\frac{(x-ng)^2}{2n\sigma_1^2}\right)
\end{aligned} \qquad (4.17)$$

[15].

Background Processes

We shall split the background processes into two groups with different distribution functions:

(I) the low charge processes present in each event (e.g. the leakage current, etc .) which are responsible for nonzero width of the signal distribution when no photoelectron was emitted from the photocathode ("Pedestal") ;

(II) the discrete processes which can, with nonzero probability, accompany the measured signal (such as thermoemission, noise initiated by the measured light, etc.). [15]

The processes of type I can be described by a Gaussian and those of type II by an exponential function. The effect of these processes when some primary photoelectrons ($n \geqslant 1$) are emitted will be discussed later. When no primary photoelectron is emitted ($n = 0$, with probability $e^{-\mu}$), the totality of the signal will be due to these backgrounds. If we call w the probability that, within these events, a background signal of type II can occour, we can parameterize the background as

$$B(x) = \frac{(1 - w)}{\sigma_0 \sqrt{2\pi}} exp\left(-\frac{x^2}{2\sigma_0^2}\right) + w\theta(x)\alpha exp(-\alpha x), \tag{4.18}$$

where σ_0 is the standard deviation of the type I background distribution, w is the probability that a measured signal is accompanied by a type II background process, α is the coefficient of the exponential de- crease of type II background, and $\theta(x)$ is the step function [15].

The Realistic Response Function of the PMT

Combining the ideal PMT spectrum and the background charge distribution we found the realistic PMT spectrum as the convolution of Eqs. 4.17 and 4.18:

$$S_{real}(x) = \int S_{ideal}(x')B(x - x')dx' \tag{4.19}$$

If noise intensity is low ($\frac{1}{\alpha} \ll g$) and μ is large ($\geqq 2$), we can replace Eq. 4.18 with the following function:

$$B(x) = \frac{1}{\sigma_0 \sqrt{2\pi}} exp\left(-\frac{(x - Q_0 - w/\alpha)}{2\sigma_0^2}\right) \tag{4.20}$$

44

[15]. Then, the PMT response function can be approximated as following [15]:

$$S_{real}(x) \approx \left\{ \frac{1-w}{\sigma_0\sqrt{2\pi}}exp\left(-\frac{(x-Q_0)^2}{2\sigma_0^2}\right) + w\theta(x-Q_0)\alpha exp[-\alpha(x-Q_0)]\right\} e^{-\mu}$$
$$+ \sum_{n=1}^{\infty} \frac{\mu^n e^{-\mu}}{n!} \times \frac{1}{\sigma_1\sqrt{2\pi n}}exp\left(-\frac{(x-Q_0-\frac{w}{\alpha}-ng)^2}{2n\sigma_1^2}\right).$$

(4.21)

[15].

4.4.3 Photon Statistics Method

First Order Approximation

Assuming that number of photons coming to PMT have a Poisson distribution, so mean value (M) and RMS (σ) of the pedestal-subtracted charge distribution of the PMT are given by:

$$M = G\mu,$$
$$\sigma = G\sqrt{\mu},$$

(4.22)

where G is the gain of PMT and μ is mean photoelectrons. Then, we can get gain and mean photoelectrons from mean and RMS in histogram:

$$\mu = (\frac{M}{\sigma})^2,$$
$$G = \frac{M}{\mu} = \frac{\sigma^2}{M}.$$

(4.23)

Or the gain and mean photoelectrons can be obtained by a Poisson fitting:

$$P_\mu(q) = A \times \frac{\mu^n \times e^{-\mu}}{n!} = A \times \frac{\mu^{\frac{q}{G}} \times e^{-\mu}}{\Gamma(\frac{q}{G}+1)},$$

(4.24)

where A is amplitude and q is measured charge for each event [16].

Second Order Approximation

In the first order approximation, we assume that photoelectron distribution is Poisson. Now, we consider the effect on each dynode. As mentioned in Section 4.4.2, number of

secondary electrons also has a Poisson distribution [14] [17] [18]. The variance is not only coming from photocathode but also from dynodes.

Assuming that G' and μ' is the measured gain and mean photoelectrons in second order approximation respectively, the RMS of photocathode and dynodes are derived as following:

$$\sigma_0 = G'\sqrt{\mu'}$$

$$\sigma_{1d} = \frac{G'}{g_1}\sqrt{\mu' g_1} = G'\sqrt{\frac{\mu'}{g_1}}$$

$$\sigma_{2d} = \frac{G'}{g_1 g_2}\sqrt{\mu' g_1 g_2} = G'\sqrt{\frac{\mu'}{g_1 g_2}} \qquad (4.25)$$

$$\dots$$

$$\sigma_{nd} = \frac{G'}{g_1 g_2 \dots g_n}\sqrt{\mu' g_1 g_2 \dots g_n} = G'\sqrt{\frac{\mu'}{g_1 g_2 \dots g_n}}$$

where σ_0 means the RMS of the Poisson fluctuation at the photocathode, σ_{nd} means the RMS of the Poisson fluctuation at the n-th dynode, and g_n is the gain of the n-th dynode. So the total variance should be

$$\begin{aligned}
\sigma^2 &= \sigma_0^2 + \sigma_{1d}^2 + \sigma_{2d}^2 + \dots + \sigma_{12d}^2 + \sigma_{ped}^2 \\
&= G'^2 \mu' \left(1 + \frac{1}{g_1} + \frac{1}{g_1 g_2} + \dots + \frac{1}{g_1 g_2 \dots g_n}\right) + \sigma_{ped}^2 \\
&= G'^2 \mu' \alpha + \sigma_{ped}^2 \qquad (4.26) \\
&= MG'\alpha + \sigma_{ped}^2 \\
&= \frac{M^2}{\mu'}\alpha + \sigma_{ped}^2
\end{aligned}$$

[17] [19], here σ_{ped} is deviation of pedestal and we define a correction coefficient α:

$$\alpha \equiv 1 + \frac{1}{g_1} + \frac{1}{g_1 g_2} + \dots + \frac{1}{g_1 g_2 \dots g_n}. \qquad (4.27)$$

In single photoelectron case, the variance σ_1^2 would be:

$$\sigma_1^2 = \sigma_{1d}^2 + \sigma_{2d}^2 + \ldots + \sigma_{12d}^2 + \sigma_{ped}^2$$

$$= G'^2 \left(\frac{1}{g_1} + \frac{1}{g_1 g_2} + \ldots + \frac{1}{g_1 g_2 \ldots g_n} \right) + \sigma_{ped}^2 \qquad (4.28)$$

$$= G'^2 (\alpha - 1) + \sigma_{ped}^2.$$

Thus, the correction coefficient α can be calculated from the standard deviation of single photoelectron and gain G':

$$\alpha = 1 + \left(\frac{\sigma_1^2 - \sigma_{ped}^2}{G'^2} \right). \qquad (4.29)$$

In most situations, σ_{ped} is usually neglected because it is much less than other terms. From Eq. 4.26 and Eq. 4.23, we found the relation between first order approximation and second order approximation:

$$\mu' = \alpha \left(\frac{M^2}{\sigma^2 - \sigma_{ped}^2} \right) \xrightarrow{\sigma \gg \sigma_{ped}} \alpha \mu,$$
$$\qquad (4.30)$$
$$G' = \frac{M}{\mu} = \frac{\sigma^2 - \sigma_{ped}^2}{\alpha M} \xrightarrow{\sigma \gg \sigma_{ped}} \frac{G}{\alpha}.$$

Thus, the gain and mean photoelectrons can be calculated with Eq. 4.30 but the question is what is the value of the correction coefficient α.

Estimate Correction Coefficient

Secondary emission gain g_i is a function of the voltage of dynodes V_i, and is given by the following equation:

$$g_n = a V_i^k, \qquad (4.31)$$

where a is a constant, k is determined by the structure and material of the dynode and usually has a value from 0.7 to 0.8. [8]

Total gain is the product of $\beta, g_1, g_2, \ldots g_i$, and the equation is as following:

$$G = \beta g_1 g_2 \ldots g_i, \qquad (4.32)$$

where β is the collection efficiency which is determined by first dynode voltage [8]. Fig. 4.7 shows the relation between collection efficiency and first dynode voltage, and formula

can be derived as following:

$$\beta(V_1) = 1 - e^{-0.04V_1} \tag{4.33}$$

First, we consider Hamamatsu HMAPMT H8500C. It has twelve dynodes which have the same supply voltage. Fig. 4.8 shows the voltage distribution ratio in MAPMT H8500C.
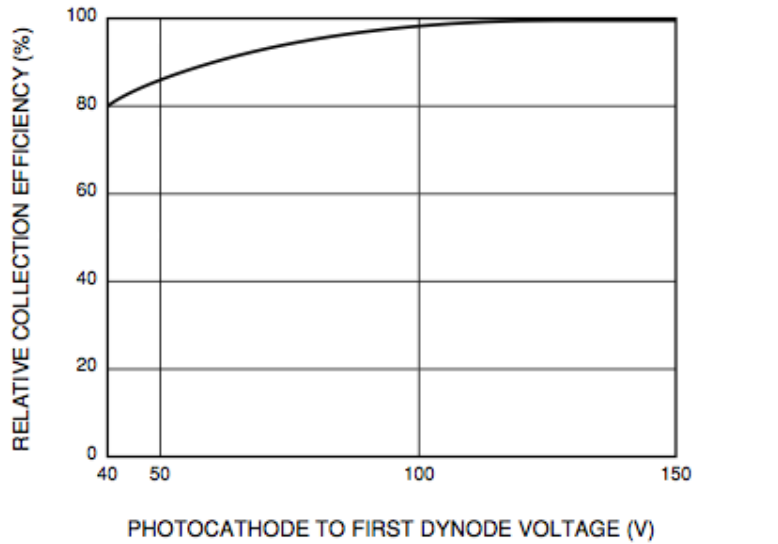

Figure 4.7: Collection efficiency vs. photocathode to first dynode voltage [8]

Electrodes	K	Dy1	Dy2	Dy3	Dy4	Dy5	Dy6	Dy7	Dy8	Dy9	Dy10	Dy11	Dy12	GR	P
Distribution Ratio	1	1	1	1	1	1	1	1	1	1	1	1	1	0.5	

Supply Voltage: -1000 V, K: Cathode, Dy: Dynode, GR: Guard Ring P: Anode

Figure 4.8: Voltage Distribution Ratio and Supply Voltage in MAPMT H8500C [9]

Thus, supply voltage at each dynode is the same and its value equals total supply voltage dividing by 13.5. Thus, gain of each dynode should be the same:

$$g_1 = g_2 = \ldots = g_{12} = aV_1^k = a\left(\frac{V}{13.5}\right)^k, \tag{4.34}$$

where V is supply voltage on MAPMT.

Substituting Eq. 4.34 into Eq. 4.32, the equation of total gain is as following:

$$G = \beta a^{12}\left(\frac{V}{13.5}\right)^{12k}. \tag{4.35}$$

48

Table 4.1: Estimated the values of dynode voltage, collection efficiency, dynode gain, and correction coefficient at different supply voltage with Hamamatsu MAPMT H8500C from data sheet

Supply voltage V (V)	700	750	800	850	900	950	1000	1050	1100
Dynode voltage V_1 (V)	51.85	55.56	59.26	62.96	66.67	70.37	74.07	77.78	81.48
Collection efficiency β	0.874	0.892	0.907	0.919	0.931	0.940	0.948	0.955	0.962
Dynode gain g_1	2.635	2.748	2.858	2.966	3.071	3.174	3.275	3.374	3.471
Correction Coefficient α	1.612	1.572	1.538	1.509	1.483	1.460	1.440	1.421	1.405

Table 4.2: Estimated the values of dynode voltage, collection efficiency, dynode gain, and correction coefficient at different supply voltage with Hamamatsu MAPMT H7546 from data sheet

V (V)	500	550	600	650	700	750	800	850	900	950	1000
V_1 (V)	68.18	75.00	81.82	88.64	95.45	102.3	109.1	115.9	122.7	129.6	136.4
β	0.935	0.950	0.962	0.971	0.978	0.983	0.987	0.990	0.993	0.994	0.996
g_1	4.016	4.375	4.730	5.082	5.431	5.778	6.123	6.465	6.805	7.143	7.479
α	1.435	1.368	1.321	1.286	1.258	1.236	1.218	1.202	1.189	1.177	1.167

From Eq. 4.35 and Fig. 2.10, $k = 0.610$ and $a = 0.237$ are calculated. Table 4.1 shows the calculation result about correction coefficient at different supply voltage for Hamamatsu MAPMT H8500C.

With the same method, coefficient k and a of Hamamatsu MAPMT H7546 are also calculated as $k = 0.897$ and $a = 0.091$. The calculated correction coefficients are shown in Table 4.2.

4.4.4 Result

Low Light Level (< 3 phe.)

To measure gain, the simplest one is to find where is the position of single photoelectron peak. But the obvious single photoelectron peak is not seen in pulse height histogram measured with our MAPMT because of lower gain at first dynode. The standard deviations of photoelectrons are too large to separate them.

The multi-Gaussian fitting method (Eq. 4.21), photon statistics method (Eq. 4.23), and Poisson fitting method (Eq. 4.24) are adopted. Function generator sent pulses, whose height is from $3.3V$ to $4.3V$ and width is $10ns$, to LED to emit light and a teflon was put in front of LED to lower light level. Hamamatsu MAPMT H8500C is drove at HV -900V. The multi-Gaussian fitting and Poisson fitting results in low light level (< 3 phe.) are shown in Fig. 4.9 and Fig. 4.10. There are 50000 events in each measurement.

Table 4.3 is the result and it shows mean photoelectrons (μ_{fit}), correction coefficient from fitting (α_{fit}), fitting gain (G_{fit}), first order approximate gain (G_{1st}), second order approximate gain (G_{2nd}), Poisson fitting gain ($G_{Poisson}$), and Poisson fitting correction gain (G_{2ndPoi}). μ_{fit} and G_{fit} are got from multi-Gaussian fitting result and according to Eq. 4.29, the correction coefficient (α_{fit}) is calculated. G_{1st} is got from substituting mean and RMS of histogram into Eq. 4.23, and then we divide it by (α_{fit}) to get G_{2nd} as Eq. 4.30. From Poisson fitting, we obtain $G_{Poisson}$, and we also divide it by (α_{fit}) then the G_{2ndPoi} is got.

In Fig. 4.9, the green line and blue line represent pedestal and background, and the others represent photoelectrons. The average of correction coefficient α_{fit} in Table 4.3 is 1.516 and the theoretical value of correction coefficient we estimate in HV -900V is 1.483 in Table 4.1. They only have about 2% difference.

G_{1st} is greater than G_{fit} in each event, but the corrected gain G_{2nd} is close to G_{fit}. The averages of G_{2nd} and G_{fit} are 232.6 and 240.3 respectively. There is about 3% difference between them.

In Fig. 4.10, Poisson doesn't fit well in very low light levels($< 2phe.$). Except them, the result of Poisson fitting G_{Poi} is similar to G_{1st}.

Table 4.3: Gain comparison in Fig. 4.9

Figure	$\mu_{fit}(phe.)$	α_{fit}	$G_{fit}(\frac{phe.}{mV})$	$G_{1st}(\frac{phe.}{mV})$	$G_{2nd}(\frac{phe.}{mV})$	$G_{Poi}(\frac{phe.}{mV})$	$G_{2nd_{Poi}}(\frac{phe.}{mV})$
(a)	0.060	1.650	211.5	428.8	289.2	605.3	336.8
(b)	0.268	1.518	225.6	339.6	229.0	131.1	86.36
(c)	0.673	1.491	231.1	329.8	222.4	204.1	136.9
(d)	1.315	1.525	236.7	330.7	216.9	302.1	198.1
(e)	1.498	1.435	246.7	320.8	223.6	318.7	222.1
(f)	2.067	1.472	243.5	332.5	225.9	333.3	226.4
(g)	2.202	1.555	256.3	320.8	223.6	343.7	221.0
(h)	2.614	1.566	255.1	326.9	208.8	337.8	215.7
(i)	3.017	1.435	256.2	320.8	223.6	342.5	238.7

μ: mean of photoelectrons

α_{fit}: correction coefficient from $(\frac{\sigma_1^2}{G^2} + 1)$

G_{fit}: Gain from multi-Gaussian fitting

G_{1st}: Gain from first-order approximate photon statistics

G_{2nd}: Gain from second-order approximate photon statistics

G_{Poi}: Gain from one Poisson fitting

$G_{2nd_{Poi}}$: Gain from one Poisson fitting and using correction coefficient

High Light Level(> 3 phe.)

The gain and mean photoelectrons had also measured in high light level (> 3 phe.). The measurements were with different intensity light at -700V by Hamamatsu MAPMT H8500C. Fig. 4.11 and 4.12 shows the multi-Gaussian fitting and the Poisson fitting respectively and Table 4.4 shows the fitting results.

The same high voltage were used in these measurement so the gain of each should
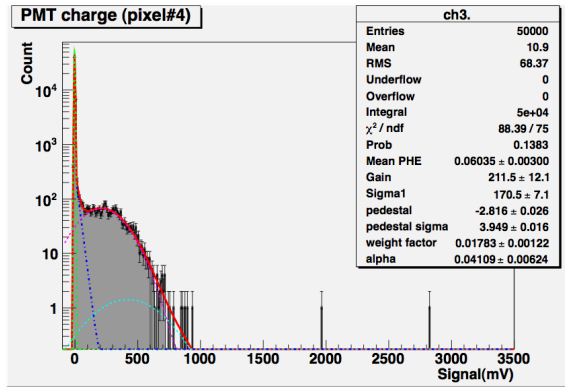
(a) HV -900V and LED 3.3V-height & 10ns-width
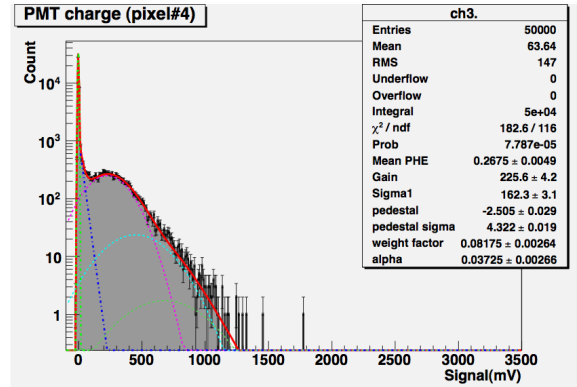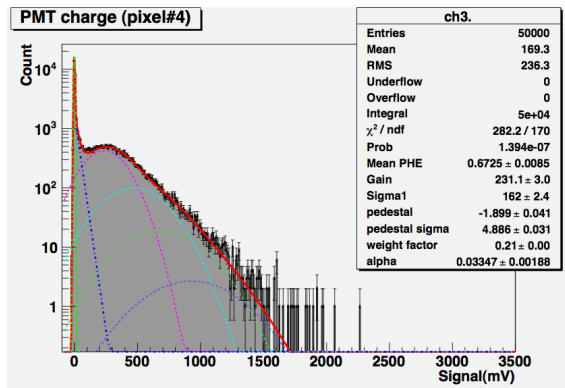
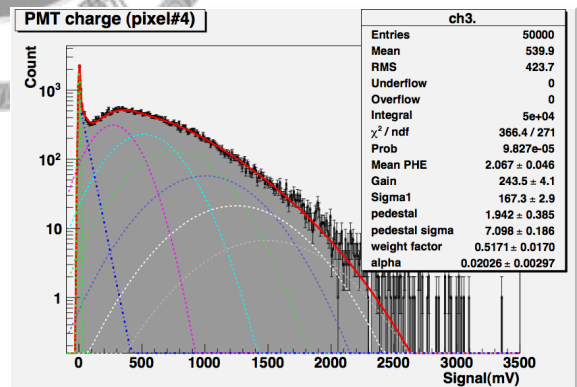(b) HV -900V and LED 3.5V-height & 10ns-width

(c) HV -900V and LED 3.7V-height & 10ns-width
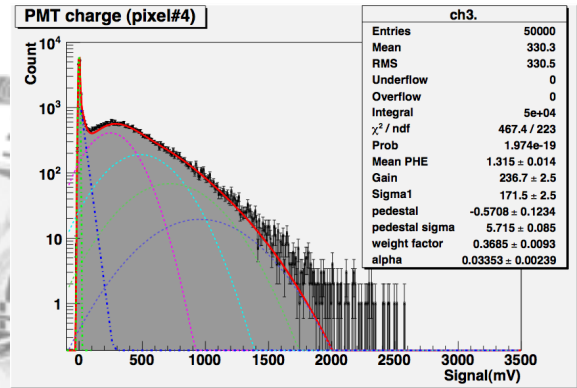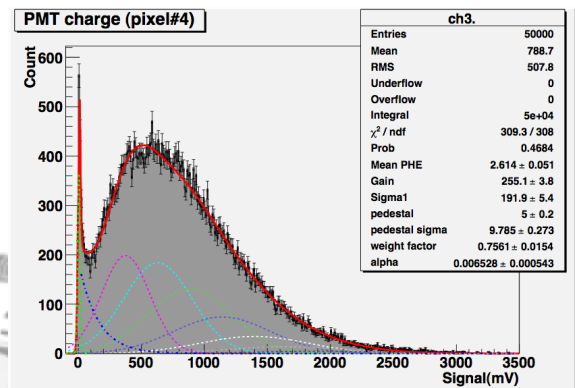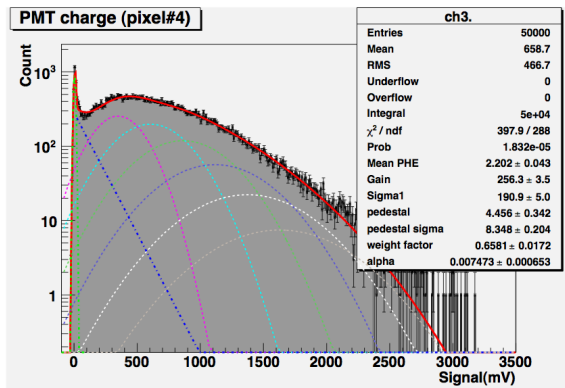
(d) HV -900V and LED 3.9V-height & 10ns-width
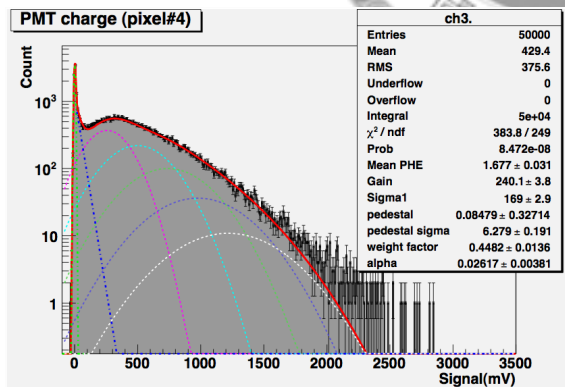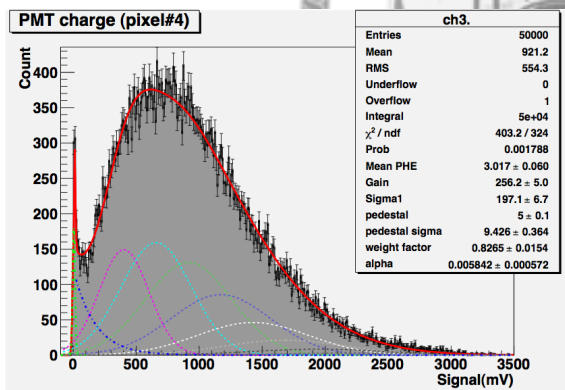
(e) HV -900V and LED 4V-height & 10ns-width

(f) HV -900V and LED 4.1V-height & 10ns-width

Figure 4.9: Multi-Gaussian Fitting results for different low light level ($< 3phe.$)with MAPMT H8500C GA1824 on HV -900V. (a) - (g) is in log scale and (h), (i) is normal scale.
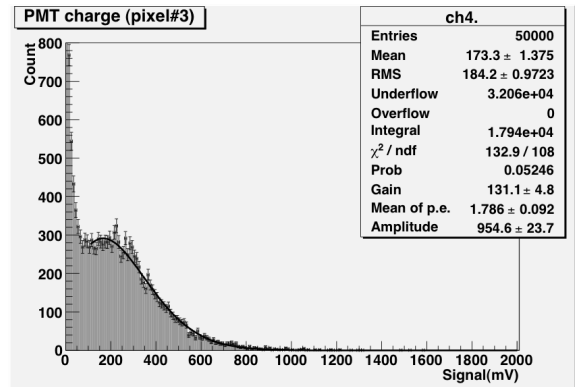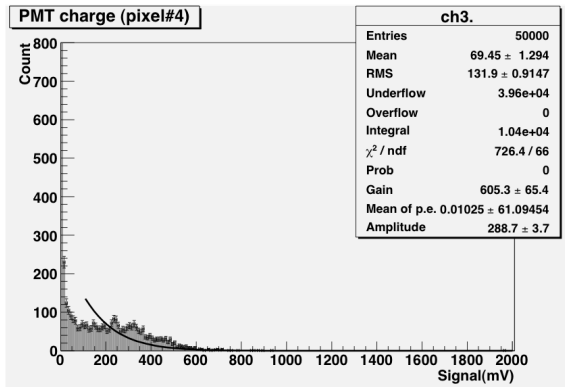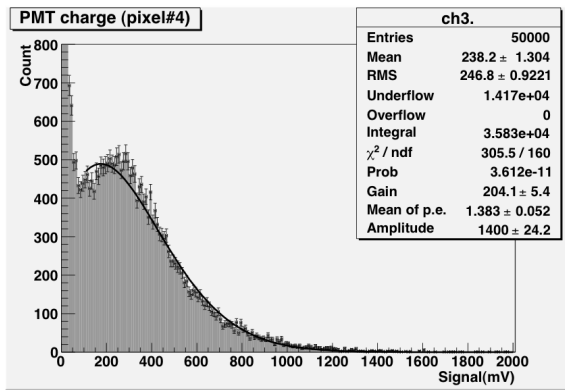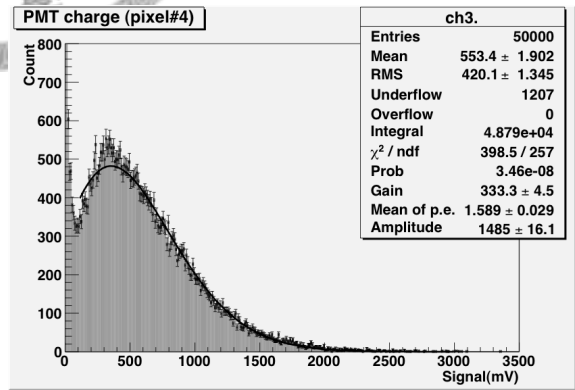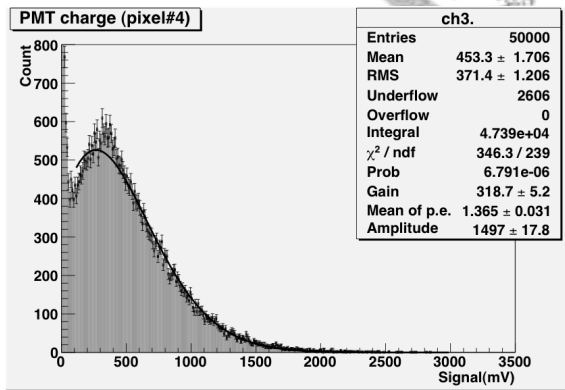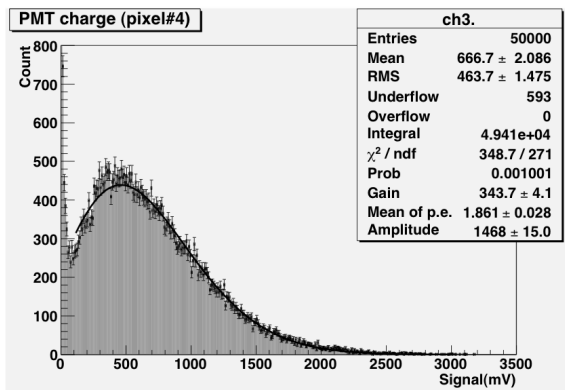
(g) HV -900V and LED 4.2V-height & 10ns-width

(h) HV -900V and LED 4.3V-height & 10ns-width

(i) HV -900V and LED 4.3V-height & 10ns-width

Figure 4.9: (continued)

(a) HV -900V and LED 3.3V-height & 10ns-width
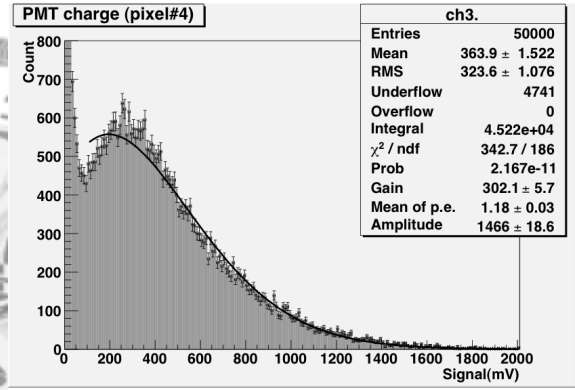
(b) HV -900V and LED 3.5V-height & 10ns-width

(c) HV -900V and LED 3.7V-height & 10ns-width

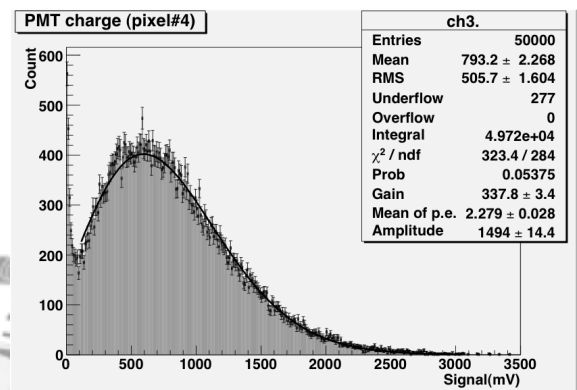(d) HV -900V and LED 3.9V-height & 10ns-width

(e) HV -900V and LED 4V-height & 10ns-width

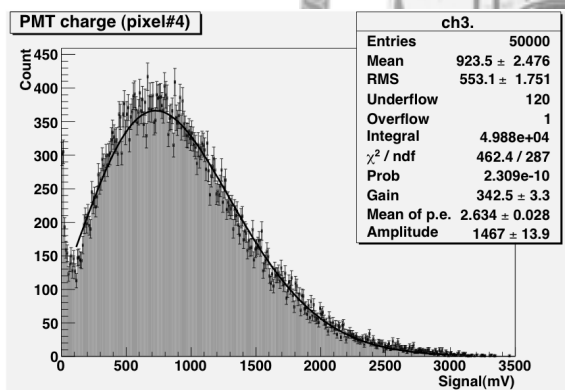(f) HV -900V and LED 4.1V-height & 10ns-width

Figure 4.10: Poisson Fitting results for different low light level ($<$ 3pe)with MAPMT H8500C GA1824 on HV -900V.

(g) HV -900V and LED 4.2V-height & 10ns-width (h) HV -900V and LED 4.3V-height & 10ns-width

(i) HV -900V and LED 4.3V-height & 10ns-width

Figure 4.10: (continued)

| Figure	$G_{fit}(\frac{phe.}{mV})$	$\mu_{fit}(phe.)$	$G_{Poi}(\frac{phe.}{mV})$	$\mu_{Poi}(phe.)$	$G_{1st}(\frac{phe.}{mV})$	$\mu_{1st}(phe.)$
(a)	29.93	3.34	54.34	2.29	53.26	2.35
(b)	26.28	4.85	49.02	3.65	49.50	3.62
(c)	28.31	8.06	45.65	7.41	46.62	7.26
(d)	32.72	12.39	45.26	11.45	46.49	11.14
(e)	38.69	17.97	44.49	15.82	45.66	15.42
(f)	38.03	23.43	44.44	20.29	45.42	19.86
(g)	36.08	28.50	44.21	24.78	45.33	24.15
(h)	36.90	35.16	44.35	29.42	45.36	28.77
(i)	38.55	38.79	44.52	33.84	45.13	33.39
(j)	44.28	38.38	44.04	38.84	44.77	38.19

Table 4.4: Gain and mean photoelectron measurement in high light level ($> 3phe.$) taken at -700 V by Hamamatsu H8500C MAPMT.

be the same. The results of G_{Poi} and G_{1st} agree this assumption except Fig. 4.12(a) and 4.12(b). But we found the gain from multi-Gaussian G_{fit} is not consistent, and also the standard deviation of single photoelectron varied in different light intensities.

The Same Light Level(≈ 4 phe.)

Here we fixed the light intensity and use different voltage which supplied to MAPMT. The pulses whose height is 4.7 V and width is 10 ns sent to LED, and the emitted light through a Teflon hit on photocathode to produce about four photoelectrons.
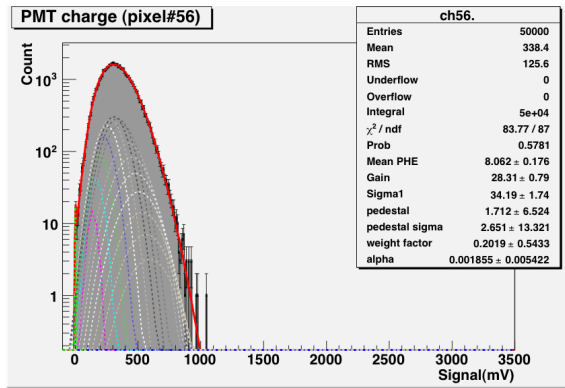
The results of fitting are shown in Table 4.5. As we expected, gain decreases when supply voltage decreases. However, mean photoelectrons also decrease when supply voltage decreases. This effect can be explained by that the collection efficiency increases
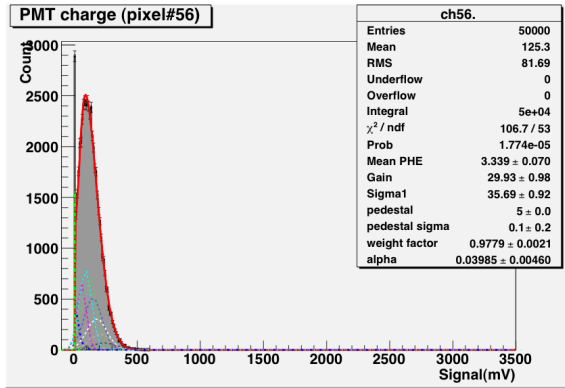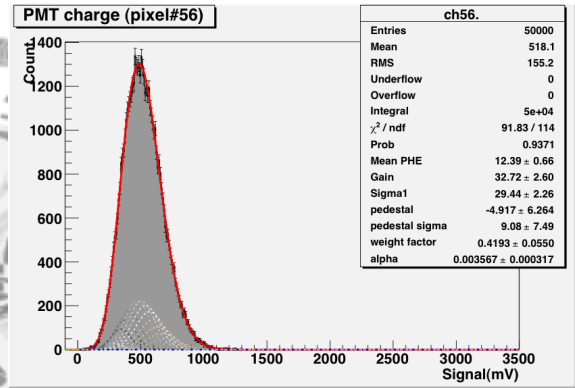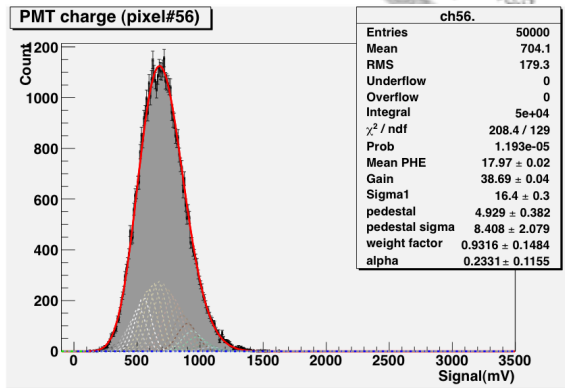
(a) LED 4.7V-height & 10ns-width
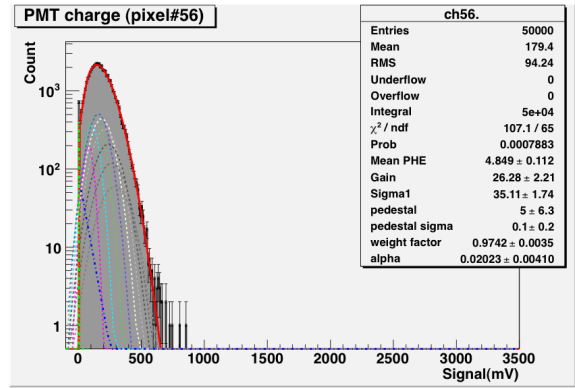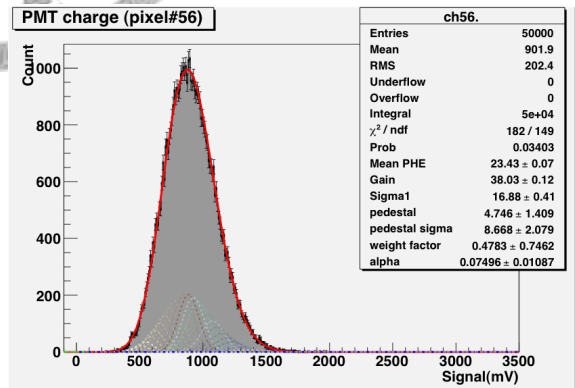
(b) LED 5V-height & 10ns-width

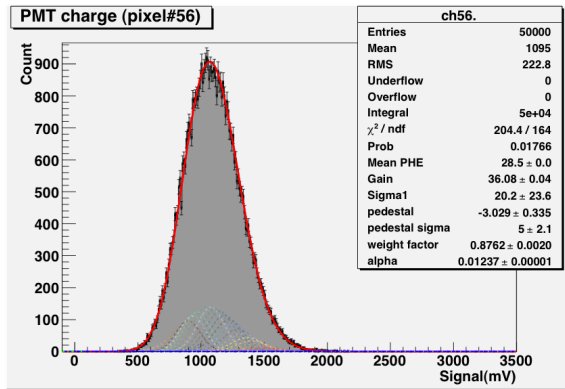(c) LED 5V-height & 12ns-width

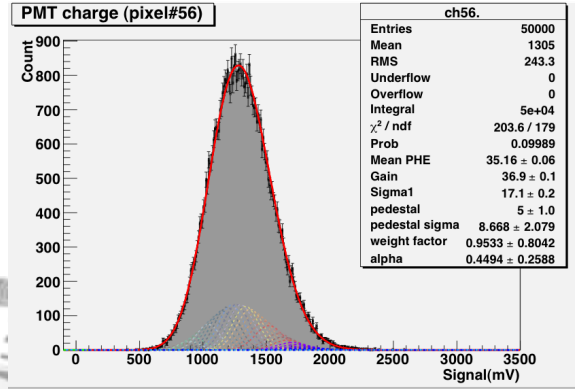(d) LED 5V-height & 14ns-width

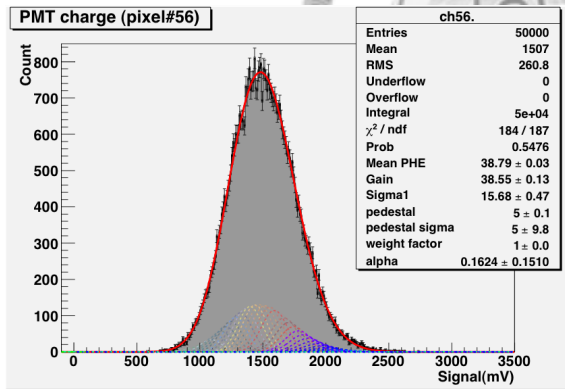(e) LED 5V-height & 16ns-width

(f) LED 5V-height & 18ns-width

Figure 4.11: Multi-Gaussian fitting results for different high light level ($>$ 3pe)with Hamamatsu MAPMT H8500C GA1824 at -700V.

(g) LED 5V-height & 20ns-width

(h) LED 5V-height & 22ns-width

(i) LED 5V-height & 24ns-width

(j) LED 5V-height & 26ns-width

Figure 4.11: (continued)

(a) LED 4.7V-height & 10ns-width

(b) LED 5V-height & 10ns-width

(c) LED 5V-height & 12ns-width

(d) LED 5V-height & 14ns-width

(e) LED 5V-height & 16ns-width

(f) LED 5V-height & 18ns-width

Figure 4.12: Poisson fitting results for different high light level ($>$ 3pe)with Hamamatsu MAPMT H8500C GA1824 at -700V.
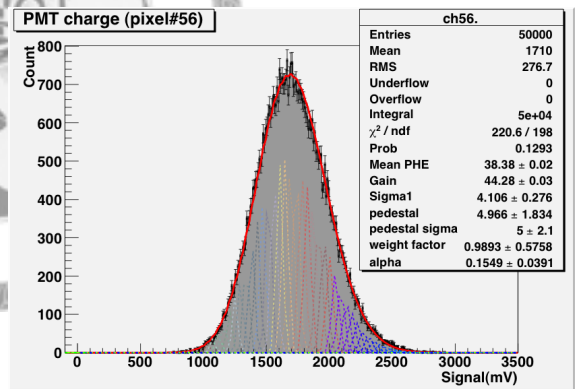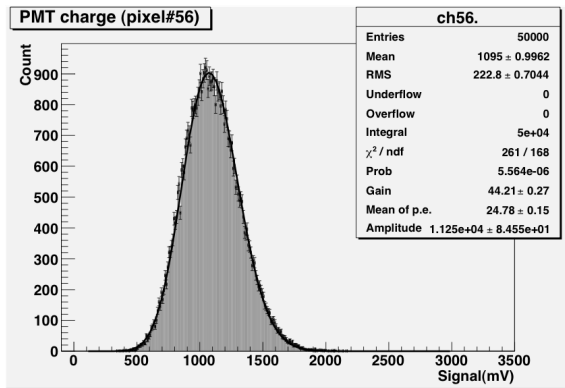
(g) LED 5V-height & 20ns-width
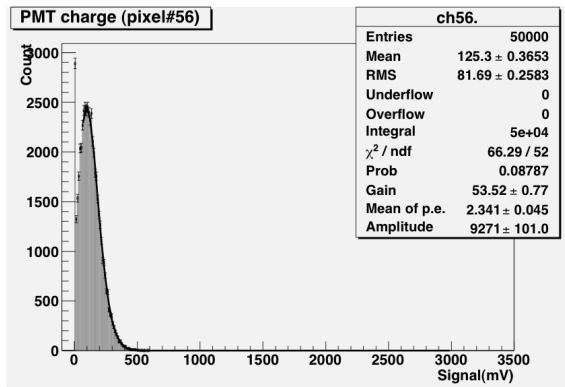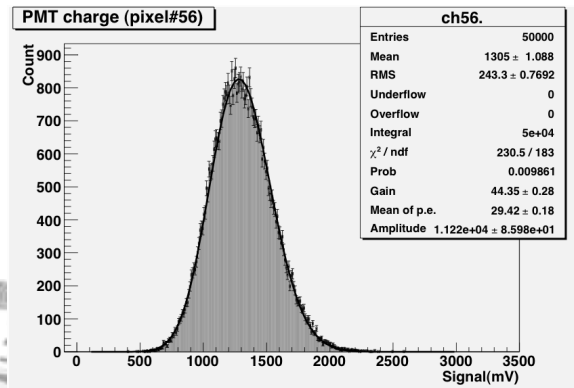
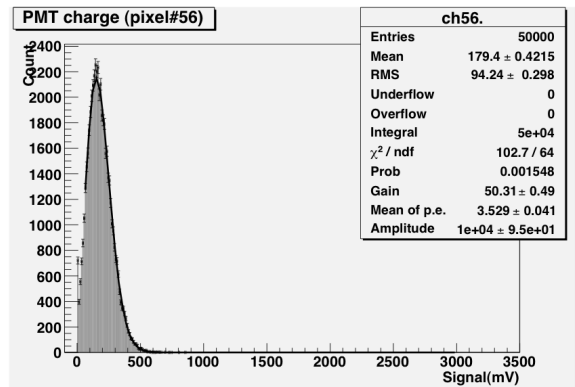(h) LED 5V-height & 22ns-width
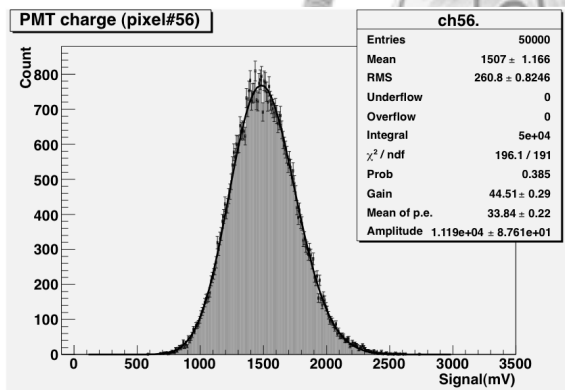
(i) LED 5V-height & 24ns-width
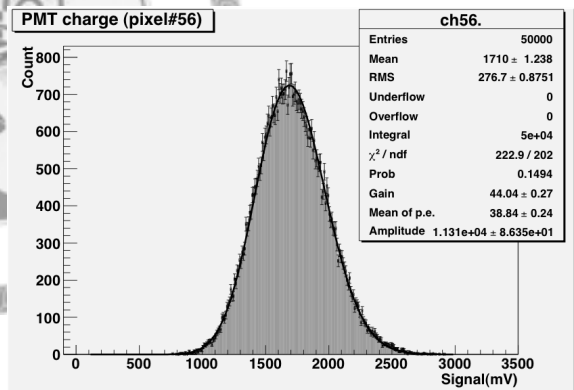
(j) LED 5V-height & 26ns-width

Figure 4.12: (continued)
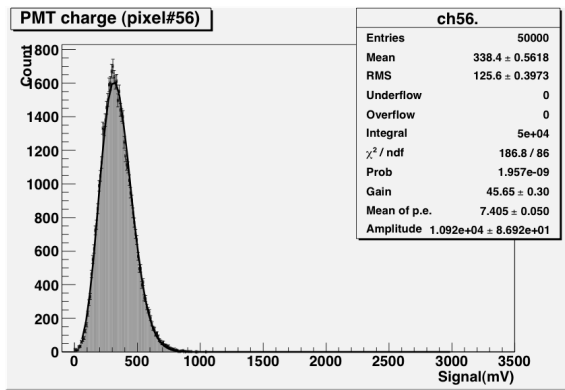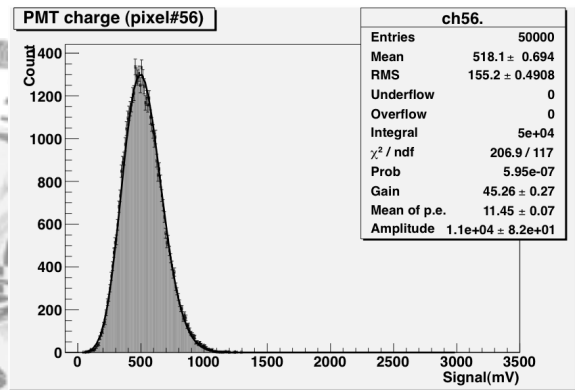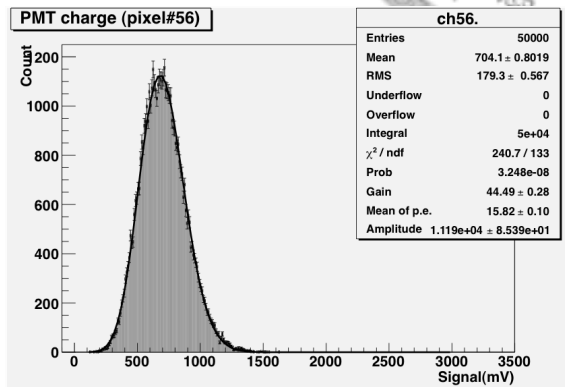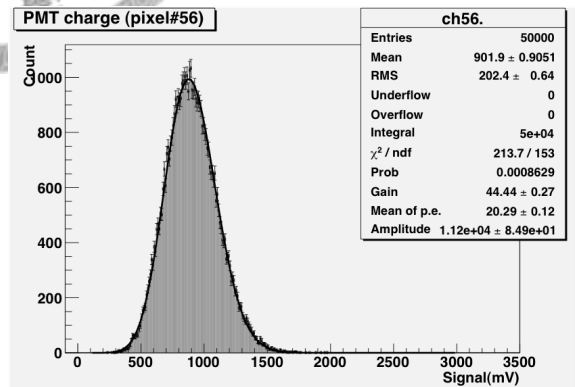
when photocathode to first dynode voltage increases.

4.5   Conclusion

We present the results showing three methods to measure gain of MAPMT. Multi-Gaussian fitting method works well in low light level and it is only way to get standard deviation of single photoelectron. But it have seven free parameters, so it is easy get bad fitting result, especially in high light level. The photon statistic method and Poisson fitting works stable except in low signal output (e.q. very low light intensity or very low gain) but if we want to get absolute values, it also need to get standard deviation of single photoelectron from Multi-Gaussian fitting method. So far, we uses these two method to measure the uniformity of MAPMT and estimate light intensity. The collection efficiency changing with supply voltage is observed in our measurement, it also be observed in Reference [20].

The single photoelectron peak is not really seen by our MAPMT. To verify our results in this section, we use HPD to observe. The detail is in the next section.
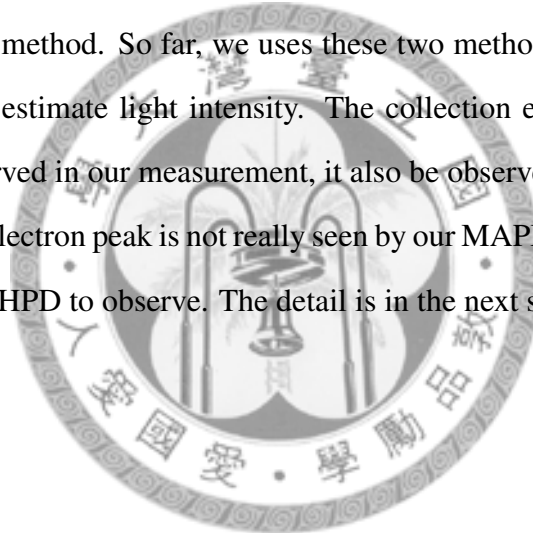
HV	$G_{fit}(\frac{phe.}{mV})$	$\mu_{fit}(phe.)$	$G_{Poi}(\frac{phe.}{mV})$	$\mu_{Poi}(phe.)$	$G_{1st}(\frac{phe.}{mV})$	$\mu_{1st}(phe.)$
-850V	142.30	4.46	204.50	3.89	207.64	3.88
-840V	111.50	4.39	186.03	3.75	188.13	3.76
-830V	139.50	3.96	169.83	3.66	169.97	3.71
-820V	121.00	4.02	153.60	3.63	153.96	3.68
-810V	103.80	4.09	137.82	3.58	136.60	3.67
-800V	97.48	3.94	123.65	3.55	122.96	3.62
-790V	69.90	4.65	110.10	3.54	108.88	3.64
-780V	75.89	3.94	99.39	3.48	99.32	3.54
-770V	53.38	4.74	88.69	3.41	87.38	3.52
-760V	52.98	4.15	77.28	3.41	76.09	3.52
-750V	42.29	4.63	70.30	3.26	69.43	3.36
-740V	47.12	3.57	62.28	3.23	61.53	3.33
-730V	34.89	3.60	55.49	3.12	53.87	3.28
-720V	32.3	3.44	49.51	3.00	47.60	3.19
-710V	27.89	3.68	43.01	2.99	42.33	3.09
-700V	25.73	3.28	38.36	2.87	37.26	3.01

Table 4.5: Gain and mean photoelectron measurement in the same level ($\approx 4phe.$) taken at from -850 V to -700V by Hamamatsu H8500C MAPMT.

Chapter 5

Photon-Counting with HPD

In previous chapter, we demonstrated three different methods to count photoelectrons by using MAPMT. In this chapter, we introduce Hybrid Photo-Detector (HPD). It is sensitive to separate photoelectrons so it is easy to confirm the photon-counting method. Thus, we used it to observe LED light and used two methods to count photoelectrons. In the end of chapter, the results of photon-counting with two kinds of photodetector are compared.
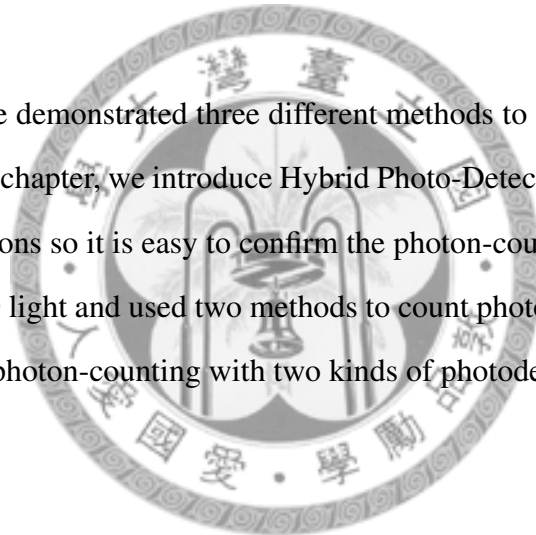
5.1   Set-up

A HPD needs two kinds of high voltages to drive. One is photocathode applied voltage which is about negative thousands Volts, and the other is avalanche diode reverse bias voltage which is about hundreds Volts. Thus, a high voltage power supply which can supply up to 10 kV was made.

The voltage signal of single photoelectron is about 2 mV with 50Ω load impedance. For purposes of measuring low light intensity level, a preamp was used to amplify signals. And a oscilloscope, whose sample rate is 5GS/s, was used to record waveforms of signals.
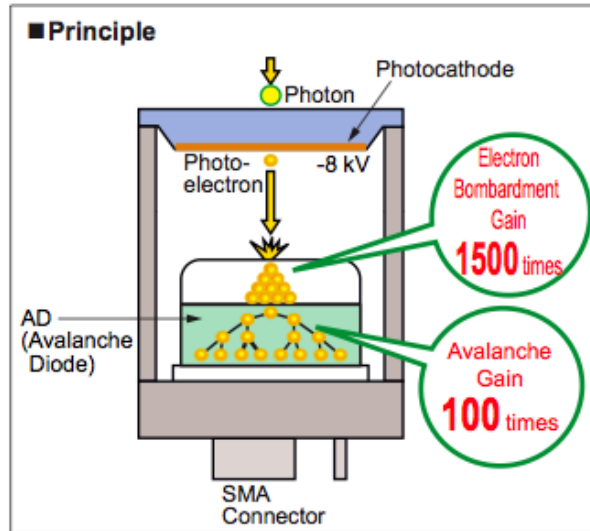
Figure 5.1: Schematics of HPD working progress [21]

5.1.1 Hybrid Photo-Detector

Fig. 5.1 shows the schematics of a Hybrid Photo-Detector (HPD). There are three main stages in HPD. First one is photoelectric effect at photocathode. The incident photons hit photocathode and the photoelectrons are emitted. At second stage, emitted photoelectrons are accelerated up to approximately 10 keV and bombard the silicon device. Then the energetic electrons deposit their kinetic energy in the silicon device and generate thousands of electron-hole pairs per bombarding electron. At final stage, Avalanche diode (AD) under AD reverse bias voltage suffers avalanche breakdown and electrons are multiplied about hundreds times [22].

The total gain of HPD is approximately 10^5 which is a little bit lower than MAPMT, but it is expected to have better pulse height resolution because there is a very large gain in first multiplication stage [22]. From Eq. 4.25, we know that the deviation which amplification process made is much low. Fig. 5.2 shows a example of pulse height distribution [8].

The HPD we used is HAMAMATSU R10467U-40. The quantum efficiency is from 30% to 45% when light waveform is from 350 nm to 700 nm.
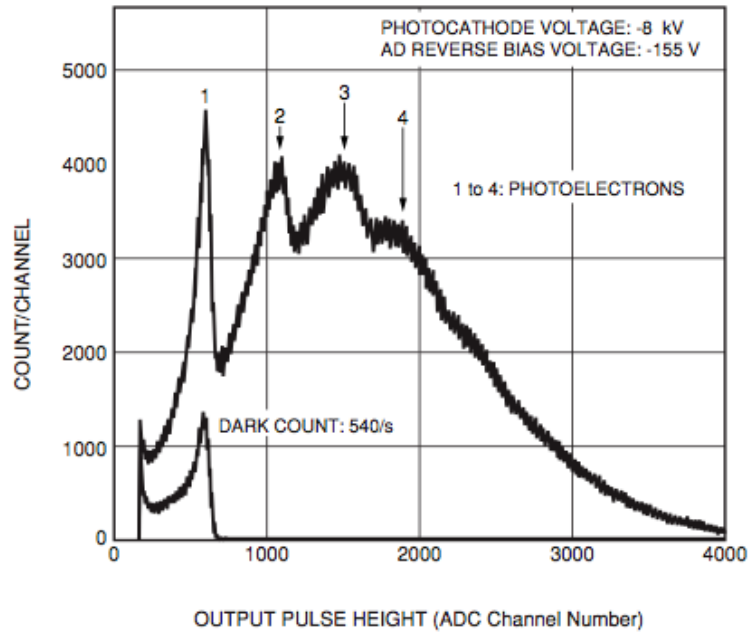
Figure 5.2: Multi-photoelectron counting characteristics [8]

5.1.2 High Voltage Power Supply

The photocathode applied voltage of HPD is up to -8500 Volts. Thus, we made a high voltage power supply, which can supply 10 kV, for photocathode voltage. Matsusada K3-10R is the HV module we used to made power supply. Figs. 5.3 and 5.4 show its picture and connection diagram. By controlling input voltage, the output high voltage can be adjusted. The control circuit design is shown in Fig. 5.5.

The stability of output voltage is measured. Figs. 5.6 and 5.7 show the stability is within 0.1% after turning on 20 minute.

5.1.3 Preamp

The voltage height of single photoelectron is about 1 mV with HPD. To reduce the noise which made in transmission, we used a preamp to amplify signal. The preamp we chose is ORTEC VT120B. It's gain is 200, and most important thing is it receive positive signals and invert them. Most preamplifiers only accept negative signals because most photode-

65

Figure 5.3: Matsusada K3-10R as HV module

CONNECTION DIAGRAM

Figure 5.4: The connection diagram of Matsusada K3-10R

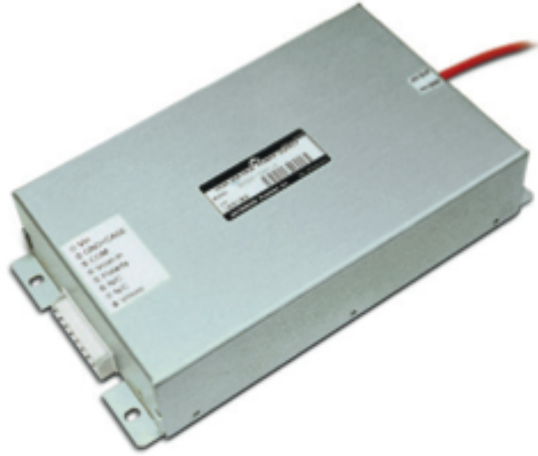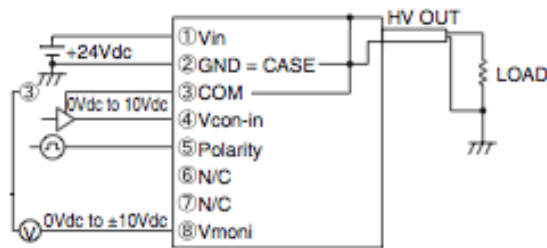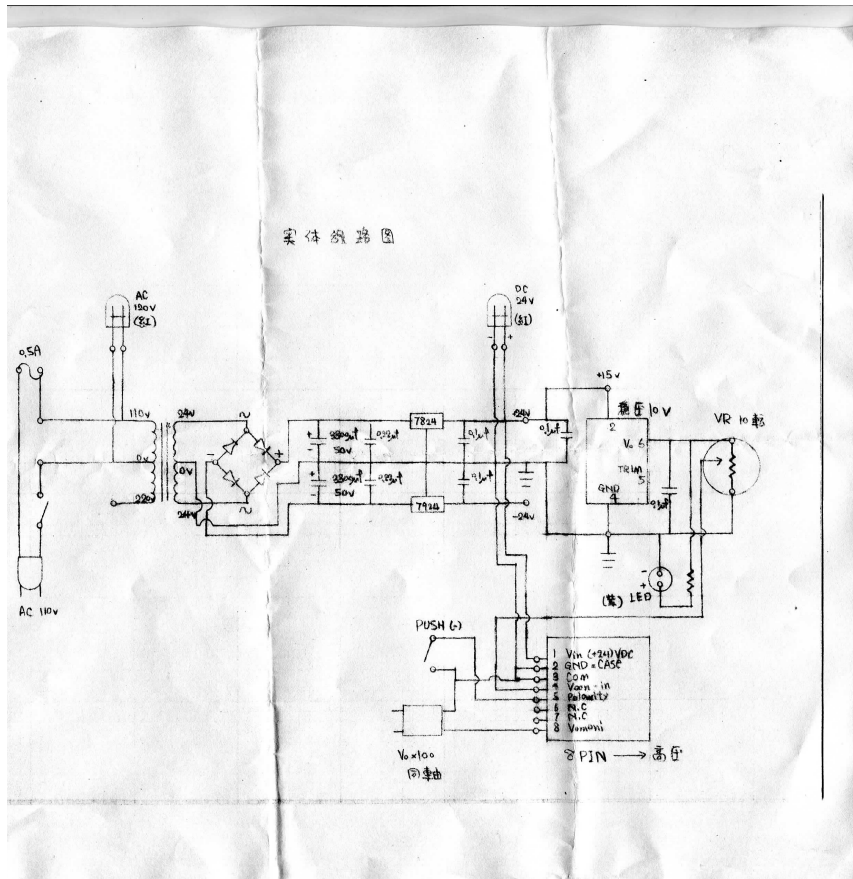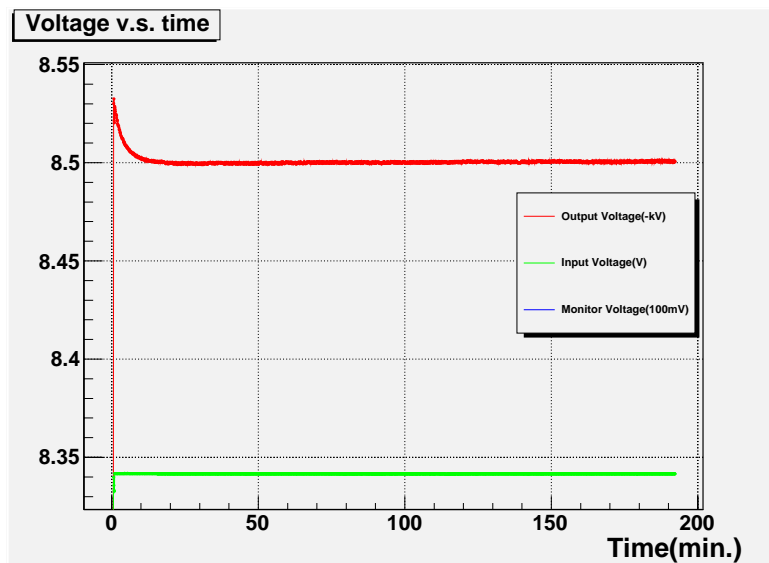Figure 5.5: The circuit diagram for high voltage power supply

Figure 5.6: Stability of high voltage power supply
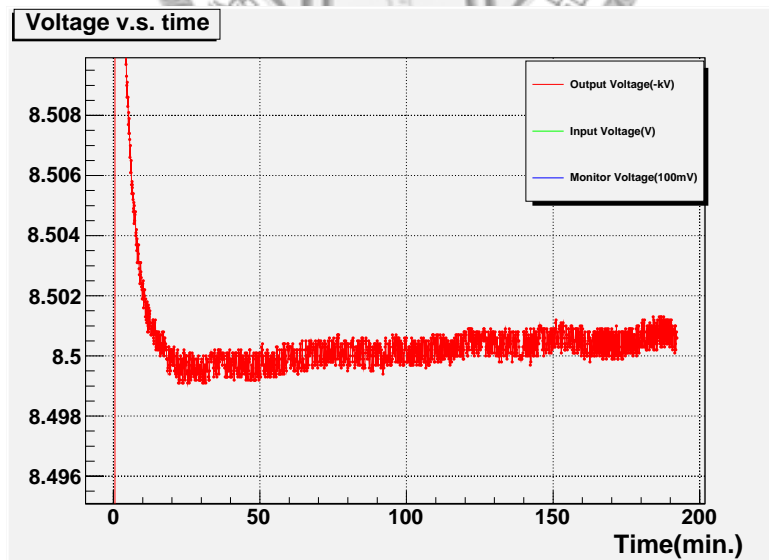
Figure 5.7: Stability of high voltage power supply

tectors output negative signals, and HAMAMATSU HPD R10467U-40 only outputs positive signals. The output range of this preamp is from 0 to -5V with 50 Ω load as shown in Fig. 5.8.

- **For amplification of signals with very fast rise times from microchannel plates, photomultiplier tubes, and silicon detectors**
- **≤1 ns rise time**
- **Output drives –5 V into 50 Ω**
- **Compact preamplifier box for operation close to the signal source**
- **≤20 µV rms equivalent input noise**
- **Gain of (A) 200, (B) –200, or (C) 20**

Figure 5.8: Preamp: ORTEC VT120

5.1.4 Readout

Tektronix DPO 4104 oscilloscope is used to catch signal. The sample rate is up to 5 GS/s and 8-bit vertical resolution, so the signal resolution is 0.04 mV and time resolution is 0.2 ns. We can use computer to control oscilloscope through a software named NI labview signalexpress tektronix edition. Thus, data can be saved through it and save rate is about $10 event/s$ when a event have 1000 points.

5.2 Selection and Integral Method

5.2.1 Event Selection

Fig. 5.9 shows a noise event has no signal. It seems have a AC signal in background and the maximum amplitude is about 0.5mV. We found that the amplitude changes with time. The height of single photoelectron is about 1 mV. To get better ratio of signal to noise, only lower noise events are selected. As shown in Fig. 5.10, we divide a event window into two regions: one is signal region and the other one is pedestal region. The RMS of

pedestal region are calculated, and we can chose a RMS cut to select events. With preamp, the signal and background are amplified. As shown in Figs. 5.11 and 5.12, the maximum amplitude is about 20mV and the height of single photoelectron is near 100 mV. So the better ratio of signal to noise is gotten with preamp.
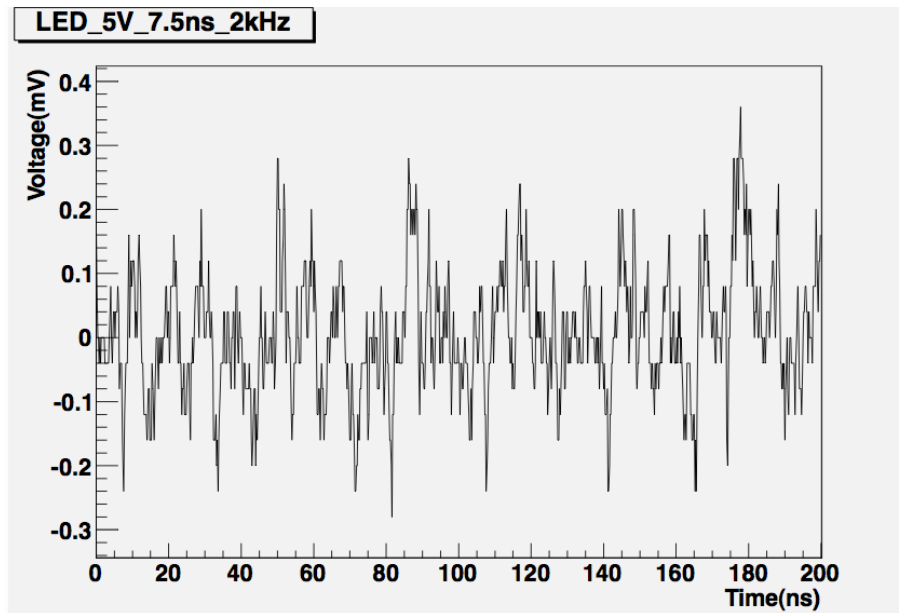
Figure 5.9: Noise event

5.2.2   Integral Method

The area of signal region in graph of voltage to time is used as photoelectron signal pulse height. Firstly, the mean pedestal is measured in background region; then in signal region, the voltage signals which subtracted pedestal are summed up as signal pulse height and the unit is $(mV \times ns)$.

5.2.3   Pulse Height Spectrum

With a pedestal RMS cut, the events which have lower noise are selected. And in each event, there is one integral pulse height. To get a pulse height spectrum, all integral pulse heights in selected events are filled in a histogram. Fig. 5.13 shows the pulse height
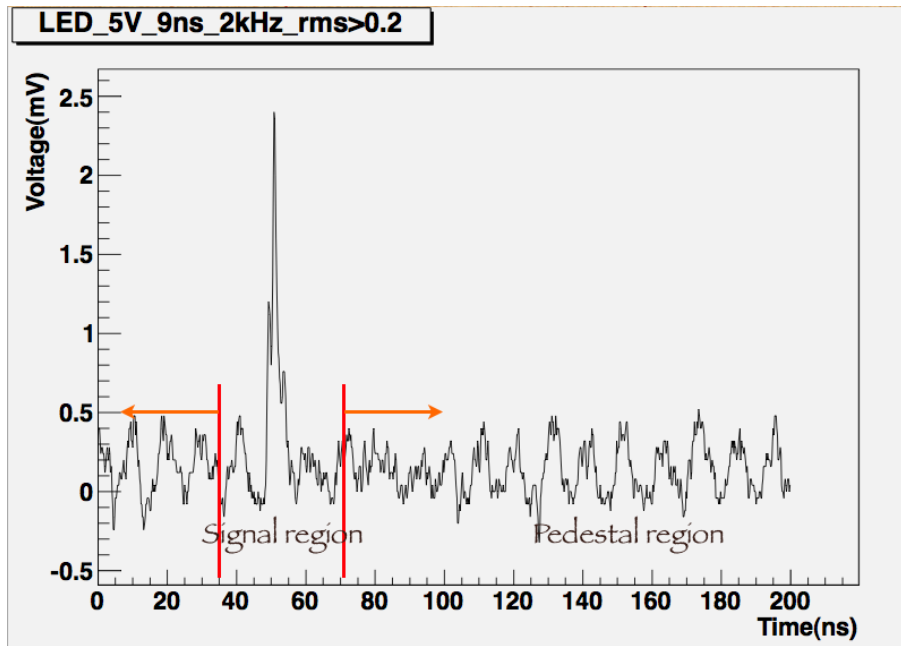
Figure 5.10: Signal region from HPD signal
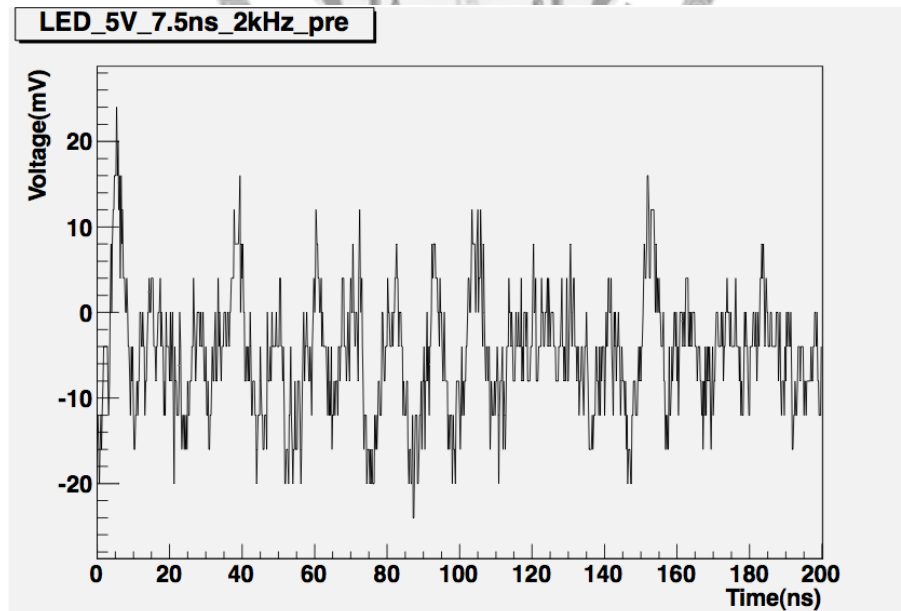
Figure 5.11: Noise event with preamp
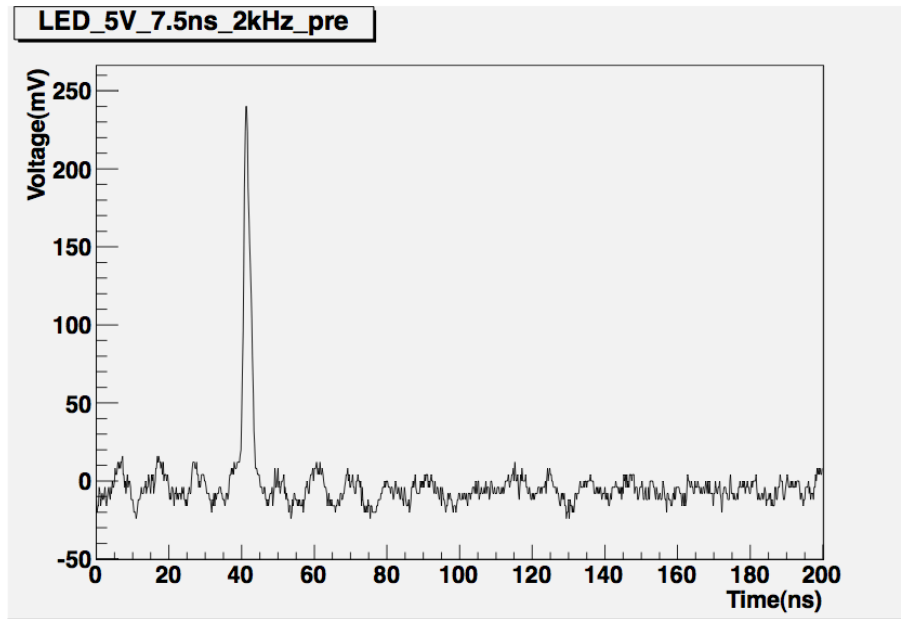
Figure 5.12: Signal region with preamp from HPD signal

spectrums with HPD. The unit of X-axis is pulse height, which is proportional to light intensity, and its unit is multiplied milivolt by nanosecond. Here, we used two different light intensities of light sources and used different pedestal RMS cut to select events. In next section, we will discuss the methods of getting gain and mean photoelectrons in these histograms.

5.3 Methods

There are two simple ways to estimate the gain and mean photoelectrons in pulse height spectrum. First one is pedestal entries ratio method. The other is photon statistics method. Both two methods base on the assumption that pulse height spectrum follows Poisson distribution.
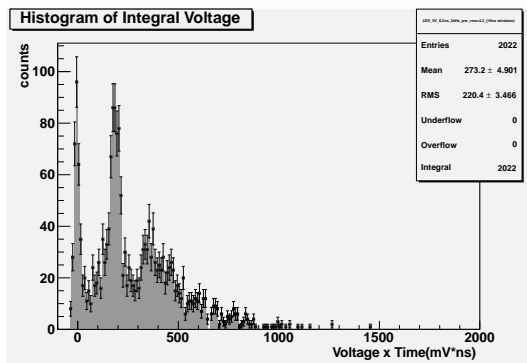
(a) 8.2ns-width. RMS < 4.3. 10ns signal window
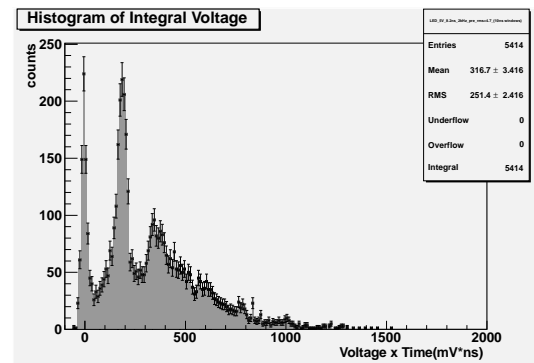
(b) 8.2ns-width. RMS < 4.7. 10ns signal window
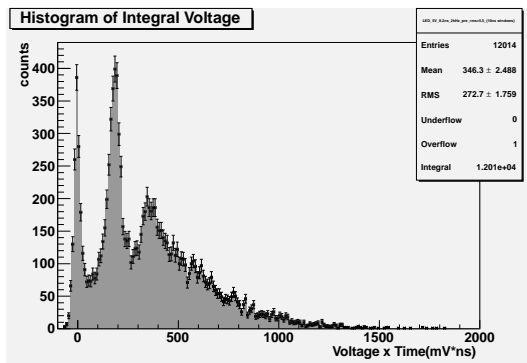
(c) 8.2ns-width. RMS < 5.5. 10ns signal window
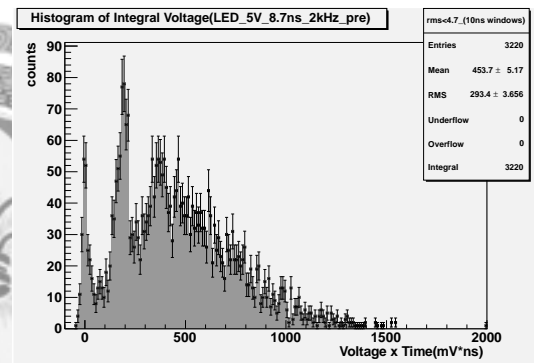
(d) 8.7ns-width. RMS < 4.7. 10ns signal window
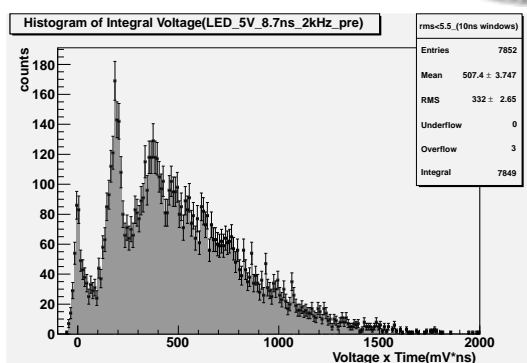
(e) 8.7ns-width. RMS < 5.5. 10ns signal window
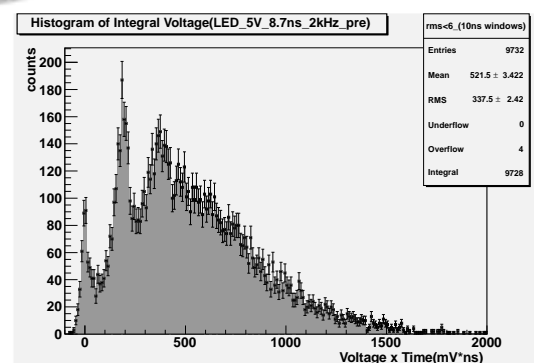
(f) 8.7ns-width. RMS < 6. 10ns signal window

Figure 5.13: Signal pulse height spectrums. The source of (a) - (c) is 5V-height, 8.2ns-width LED, and (d) - (f) is 5V-height, 8.7ns-width LED with different RMS selecting

73

events.

5.3.1 Pedestal Entries Ratio Method

As shown in Fig. 5.14, pedestal and photoelectron signals are obviously separated by a gap. We divided histogram into pedestal part and photoelectron part and got entries of pedestal part. According to Section 4.4.2 mentioned, the distribution of photoelectrons which are produced at photocathode is a Poisson distribution. Therefore, the probability of no photoelectrons produced is obtained from substituting $n = 0$ into Eq. 4.14:

$$
\begin{aligned}
P_3(n = 0; \mu) &= \frac{(\mu)^0}{0!} e^{-\mu}, \\
&= e^{-\mu},
\end{aligned}
$$

(5.1)

where μ is mean number of photoelectrons. In the histogram, pedestal probability equals ratio of pedestal entries to total entries:

$$
P_3(n = 0; \mu) = \frac{E_{ped}}{E_{total}} = e^{-\mu},
$$

where E_{ped} is entries of pedestal parts and E_{total} is total entries. Thus, mean photoelectrons are obtained as following:

$$
\mu_{PER} = ln \left(\frac{E_{total}}{E_{ped}} \right).
$$

(5.2)

So the gain is obtained as mean dividing by mean photoelectrons:

$$
G_{PER} = \frac{M}{\mu_{PER}}.
$$

(5.3)

### 5.3.2 Photon Statistics Method

As mentioned before, first multiplication determines deviation of photoelectron distribution. The first multiplication g_1 in our HPD is larger than a thousand when photocathode voltage exceeds 6 kV. Substituting g_1 into Eq. 4.27, we found that the correction coefficient $\alpha \approx 1$.

In Fig. 5.15, a Gaussian was used to fit in pedestal region and the deviation of pedestal was gotten. Comparing σ_{ped} with σ, we found $\sigma^2 \gg \sigma_{ped}^2$. So from Eq. 4.23 and

4.30, the mean photoelectron and gain can be obtained as following:

$$\mu_{PSM} \simeq \left(\frac{M}{\sigma}\right)^2, G_{PSM} \simeq \frac{\sigma^2}{M}.$$

(5.4)
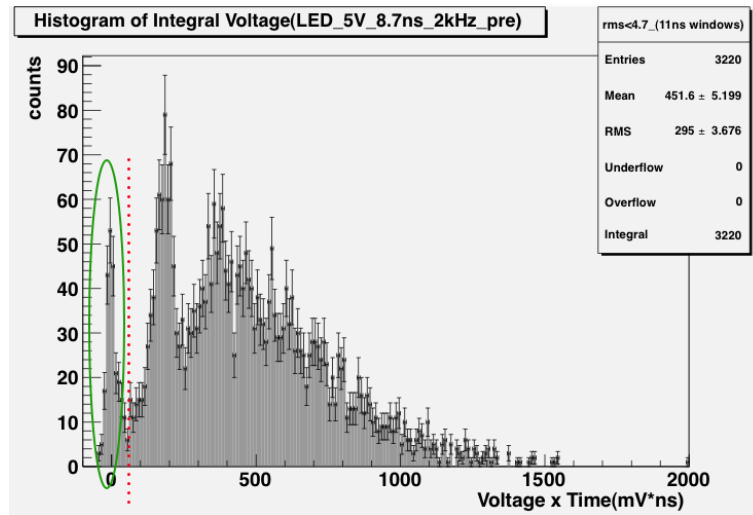
Figure 5.14: Divide histogram into pedestal part and photoelectron part.
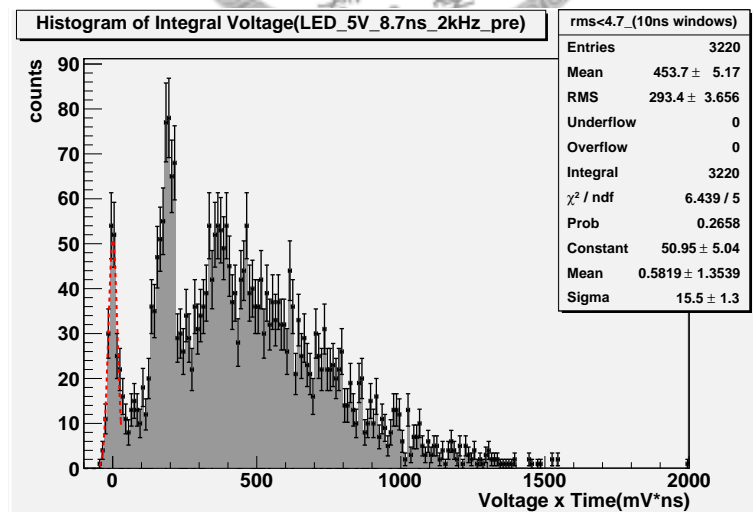
Figure 5.15: Gaussian fitting at pedestal part

75

5.4 Result

Fig. 5.13 shows separated photoelectrons' peaks, and the value of single photoelectron peak is about 180 $(mV \times ns)$. As mentioned in Section 5.3, we adopted two methods to confirm it. From Eqs. 5.2 and 5.4, the mean photoelectrons and gain can be obtained and the results are shown in Tables. 5.2 and 5.1.

In Table. 5.2, the light source is a LED light with 5V-height and 8.2ns-width pulse; In Table 5.1, the light source is a LED light with 5V-height and 8.7ns-width pulse. The window in the table means the region we integral voltage signals, and it is usually set larger than duration of light source. The RMS in the table is the RMS of pedestal, and it is used to select events.

The average of G_{PER} is 176.69, and this is close to position of single photoelectron peak. We found that G_{PSM} is always greater than G_{PER} in each measurement and G_{PSM} increases as the RMS increases. It is not surprised because in Eq. 5.4 we consider the total variance only include variance of multiplication and pedestal. But there should be some other variances, which include background noise, so G_{PSM} are always greater than real value.

Table 5.1: Gain measurement with two methods. Light source is LED with 5V-height and 8.7-width.

Window(ns)	RMS	E_{total}	E_{ped}	μ_{PER}	μ_{PSM}	G_{PER}	G_{PSM}
9	4.7	3220	238	2.60	2.48	173.40	182.27
9	5.1	5768	373	2.74	2.42	178.29	202.02
9	5.5	7852	477	2.80	2.41	180.05	209.18
9	6.0	9732	537	2.90	2.46	178.76	210.27
10	4.7	3220	247	2.57	2.39	176.70	189.72
10	5.1	5768	389	2.70	2.34	182.12	210.21
10	5.5	7852	496	2.76	2.34	183.73	217.20
10	6.0	9732	563	2.85	2.39	182.98	218.48
11	4.7	3220	253	2.54	2.34	177.53	192.70
11	5.1	5768	400	2.67	2.30	183.24	212.83
11	5.5	7852	511	2.73	2.29	185.15	220.47
11	6.0	9732	583	2.81	2.35	184.77	221.78

Window: integral signal region

RMS: selection cut

E_{total}: Total Entries

E_{ped}: Pedestal Entries

μ_{PER}: Mean photoelectrons from Pedestal Entries Ratio Method

μ_{PSM}: Mean photoelectrons from Photon Statistics Method

G_{PER}: Gain from Pedestal Entries Ratio Method

G_{PSM}: Gain from Photon Statistics Method

Table 5.2: Gain measurement with two methods. Light source is LED with 5V-height and 8.2-width.

Window(ns)	RMS	E_{total}	E_{ped}	μ_{PER}	μ_{PSM}	G_{PER}	G_{PSM}
9	4.3	2022	369	1.70	1.61	162.21	170.90
9	4.7	5414	851	1.85	1.66	172.27	191.55
9	5.1	9088	1359	1.90	1.67	178.14	202.64
9	5.5	12014	1713	1.95	1.68	178.59	206.86
9	6.0	14722	1955	2.02	1.71	178.35	210.13
10	4.3	2022	376	1.68	1.54	162.39	177.81
10	4.7	5414	866	1.83	1.59	172.81	199.49
10	5.1	9088	1385	1.88	1.60	178.93	210.00
10	5.5	12014	1757	1.92	1.61	180.15	214.76
10	6.0	14722	2012	1.99	1.65	180.30	218.08
11	4.3	2022	387	1.65	1.49	162.55	180.70
11	4.7	5414	882	1.81	1.54	172.22	202.55
11	5.1	9088	1413	1.86	1.56	178.61	213.19
11	5.5	12014	1797	1.90	1.57	180.15	218.04
11	6.0	14722	2059	1.97	1.60	180.48	221.43
12	4.3	2022	395	1.63	1.45	163.43	183.86
12	4.7	5414	894	1.80	1.51	172.50	205.73
12	5.1	9088	1432	1.85	1.53	178.87	216.31
12	5.5	12014	1819	1.89	1.54	180.30	221.26
12	6.0	14722	2086	1.95	1.57	180.76	224.63

5.5 Comparison with MAPMT

In previous two sections, photoelectron-countings with MAPMT and HPD were mentioned. In this section, we will compare the counting number of MAPMT to one of HPD with the same light source. The number of photoelectron $N_{P.E.}$ is as following:

$$\phi_{photon} \times t \times A_{effective} \times Q_{quam} = N_{P.E.}, \tag{5.5}$$

where ϕ_{photon} is photon flux, t is duration of shining, $A_{effective}$ is the effective receive area, and Q_{quam} is quantum efficiency of photodetector.

When we send pulses which have fixed height and width to LED, ϕ_{photon} and t should be constant. Thus, photon number per unit area $\phi_{photon} \times t$ should be also constant even different photodetectors are used to observe. Here we did some calculations to estimate the value of photon flux by time. The numbers should be similar if our gain measurement is right. The equation is as following:

$$\phi_{photon} \times t = \frac{N_{P.E.}}{A_{effective} \times Q_{quam}}. \tag{5.6}$$

From the data sheets, the effective area of HAMAMATSU H7546 is:

$$A_{MAPMT} = 2.0 \times 2.0 = 4.0 mm^2, \tag{5.7}$$

and the effective area of HPD is:

$$A_{HPD} = \pi \times (0.15)^2 = 7.07 mm^2. \tag{5.8}$$

The wavelength of our LED is about 400 nm. According to data sheet, the quantum efficiency of H7546 Q_{MAPMT} is about 24% and the one of HPD Q_{HPD} is about 34%. Thus, Eq. 5.9 shows the relation between photon number per unit area $\phi_{photon} \times t$ and measured photoelectron number in two kinds of photodetector .

$$
\begin{aligned}
(\phi_{photon} \times t)_{MAPMT} &= \frac{N_{P.E.}}{4.0 \times 0.24}(P.E./mm^2) \\
&= \frac{N_{P.E.}}{0.96}(P.E./mm^2) \\
(\phi_{photon} \times t)_{HPD} &= \frac{N_{P.E.}}{7.07 \times 0.34}(P.E./mm^2) \\
&= \frac{N_{P.E.}}{2.40}(P.E./mm^2)
\end{aligned} \tag{5.9}
$$

Table 5.3: photons per unit area comparison

| Light source	N_{PMT}	N_{HPD}	$(\phi t)_{PMT}(\frac{P.E.}{mm^2})$	$(\phi t)_{HPD}(\frac{P.E.}{mm^2})$
8.2ns	0.892	1.851	0.929	0.770
8.7ns	1.462	2.723	1.523	1.133
10ns	2.029	5.531	2.114	2.301
13ns	4.208	12.44	4.383	5.176

Table. 5.3 shows the calculated photon number per unit area with MAPMT and HPD in different light levels. The result shows they have about 20 - 30% difference.

5.6 Conclusion

Even there is some ground noise, we have observed single photoelectron peak. And using two methods, gain and number of photoelectron are measured.

So far, we have implemented the gain measurement of our MAPMT. Furthermore, the single photoelectron peak is observed with HPD and it confirms our fitting method. So the light intensity can be measured with NuTel readout system.
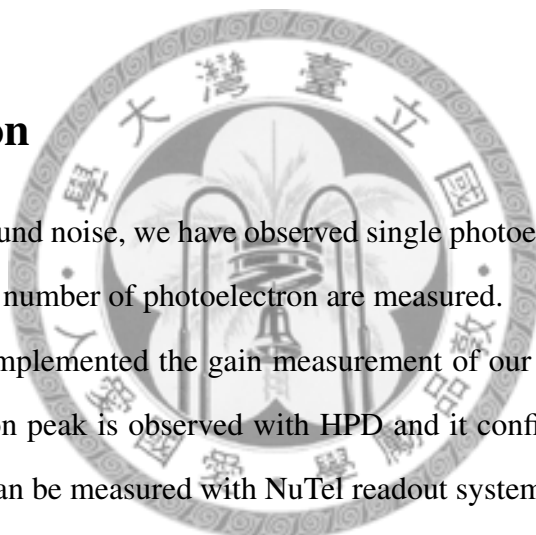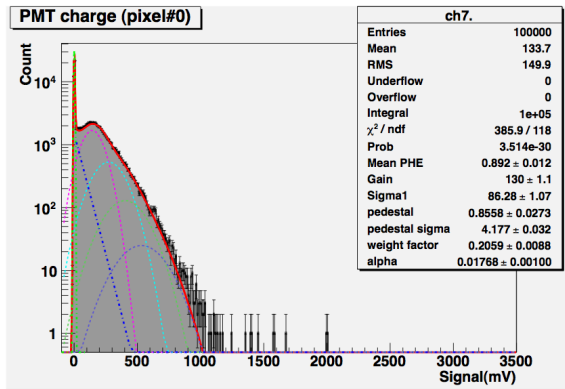
(a) LED 5V-height, 8.2ns-width with MAPMT
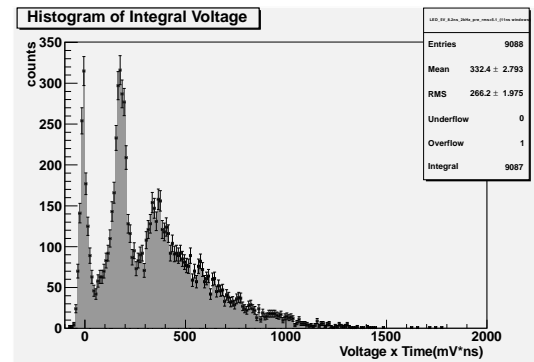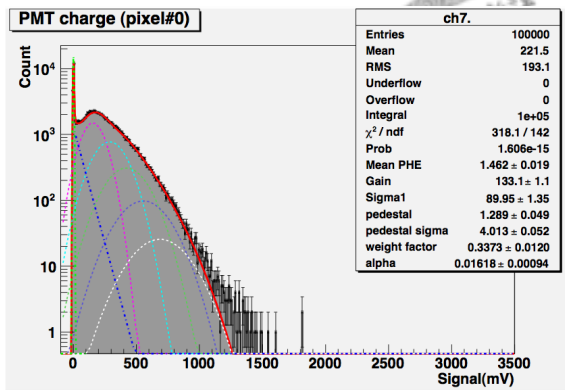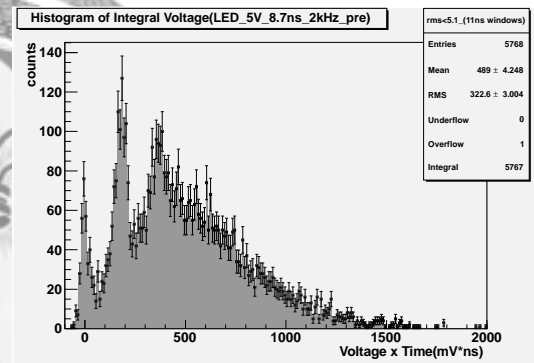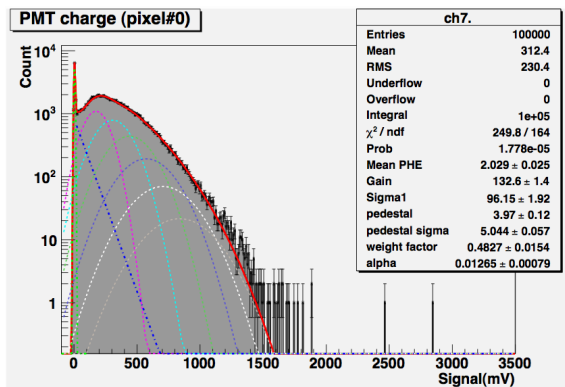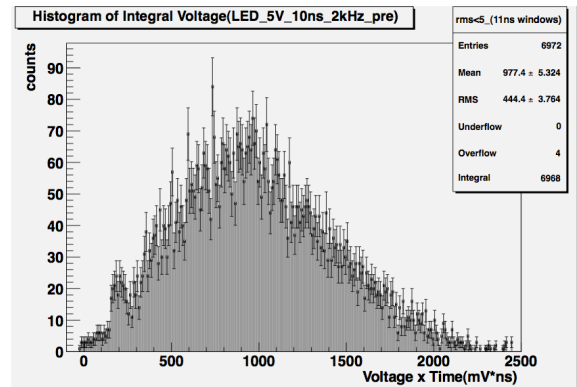
(b) LED 5V-height, 8.2ns-width with HPD

(c) LED 5V-height, 8.7ns-width with MAPMT

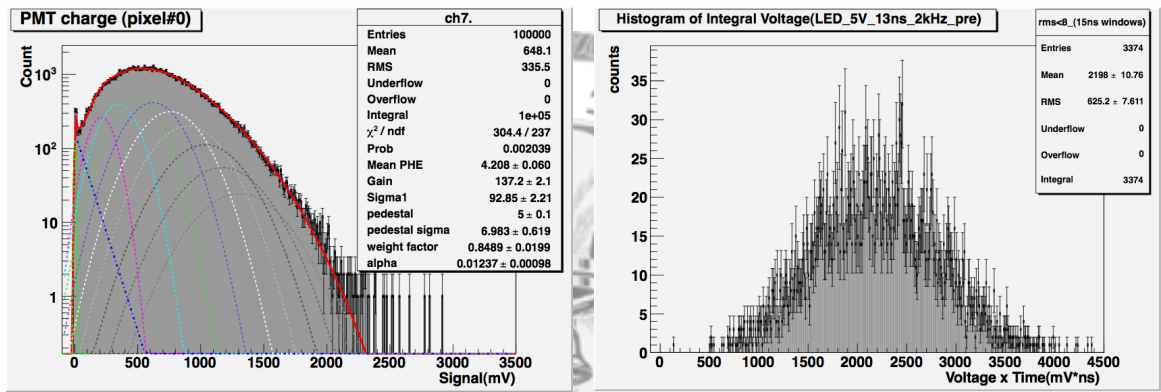(d) LED 5V-height, 8.7ns-width with HPD

(e) LED 5V-height, 10ns-width with MAPMT

(f) LED 5V-height, 10ns-width with HPD

Figure 5.16: Pulse Height Histogram of 4 light levels measured by MAPMT and HPD

(g) LED 5V-height, 13ns-width with MAPMT (h) LED 5V-height, 13ns-width with HPD

Figure 5.16: (continue)

Chapter 6

Photon-Counting in Night Sky

Background Measurement

6.1 N.S.B. at Mei-fong

In '09 July, the first NuTel field test was carried out in Mei-Fong. One telescope and corresponding read-out system, which included 4 MAPMTs, 16 pre-amps, and 1 DAQ, are delivered in Mei-Fong farm. The target mountain is Chi-Lai Mountain. The observation was done in moonless nights. We applied the calibration of MAPMT to estimate the light intensities of night sky background. The detail procedure of this measurement shows in Reference [23].

6.2 Photon Flux

Fig. 6.1 shows the triggered channel distribution in 4 MAPMTs. It is obvious to see there are several hot channels. The reason why only few channels were triggered is that gains are not uniform. So even we set the same threshold at each channel but the photoelectrons
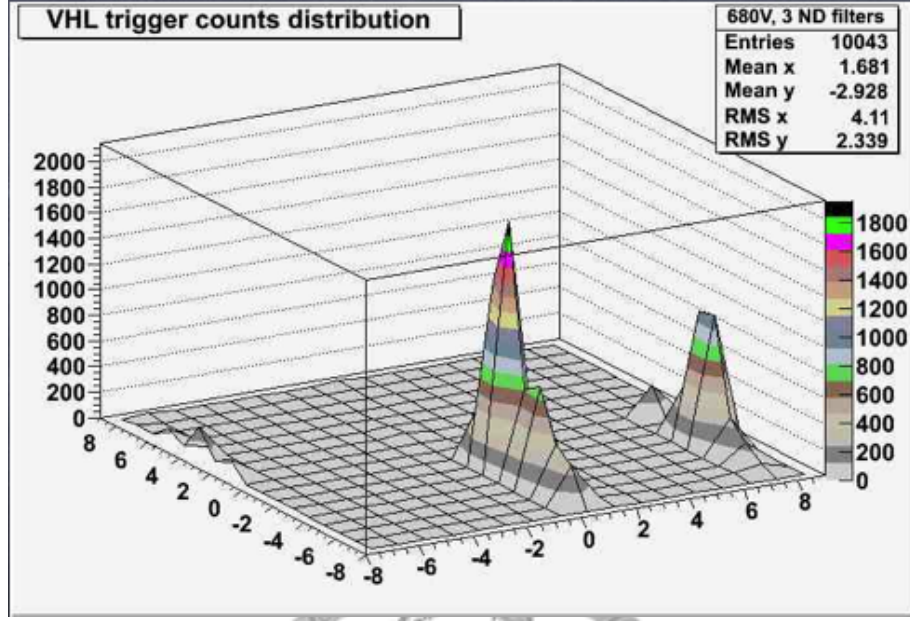
which thresholds correspond are not the same.

Figure 6.1: Triggered channel distribution in total 256 channels

The photoelectron distribution of triggered events are shown in Fig. 6.2. Total 10000 triggered events in 256 channels are measured within the interval of 99 sec, so the trigger rate is about 100 Hz. In Fig. 6.2, the red line is the threshold cut and the corresponding photoelectrons is about 5 photoelectrons. It means we missed some low light level events.

The photon flux can be obtained as following equation:

$$\phi_{photon} = \frac{N_{P.E.}}{t} \times \frac{1}{Q_{MAPMT}} \times \frac{1}{E_{opt}} \times \frac{1}{T_{BG3}} \times \frac{1}{A_{opt}} \times \frac{1}{\Omega_{pixel}}, \qquad (6.1)$$

where ϕ_{photon} is photon flux, $N_{P.E.}$ is number of photoelectron measured by photodetector, Q_{MAPMT} is quantum efficiency of photodetector (24%), E_{opt} is the transmittance of optical system (76.6% [6]), T_{BG3} is the transmittance of BG3 (80%), A_{opt} optical receive area ($0.56^2\pi\ m^2$), and Ω_{pixel} is the solid angle in each pixel $(0.5°)^2$.

Thus, the photon flux of triggered events can be estimate as following:

$$\phi_{photon} = \frac{6.535 \times 1.612}{200} \times \frac{1}{0.24} \times \frac{1}{0.766} \times \frac{1}{0.80} \times \frac{1}{0.56^2\pi} \times \frac{1}{(0.5°)^2}$$
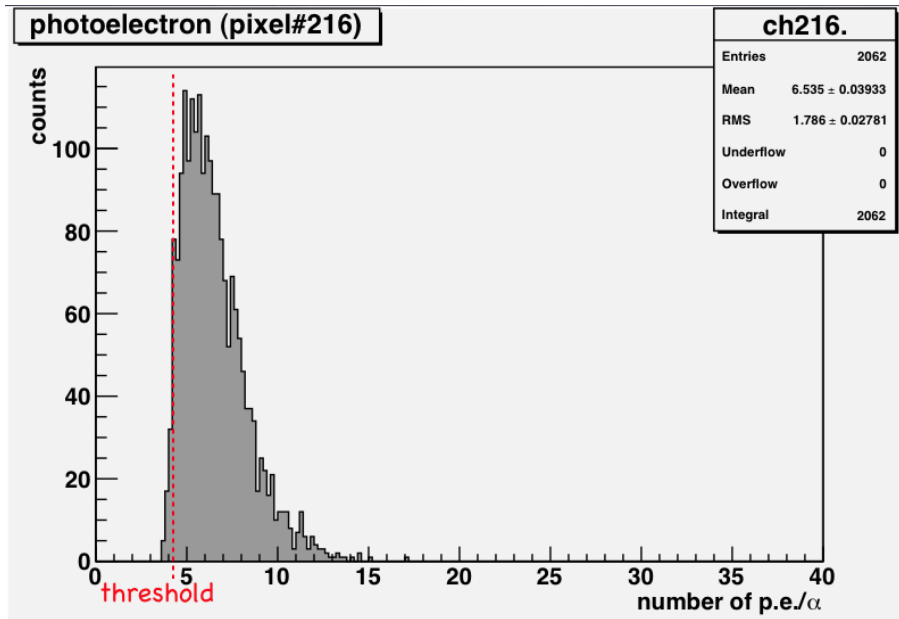$$= 4773 m^{-2}sr^{-1}ns^{-1} \qquad (6.2)$$

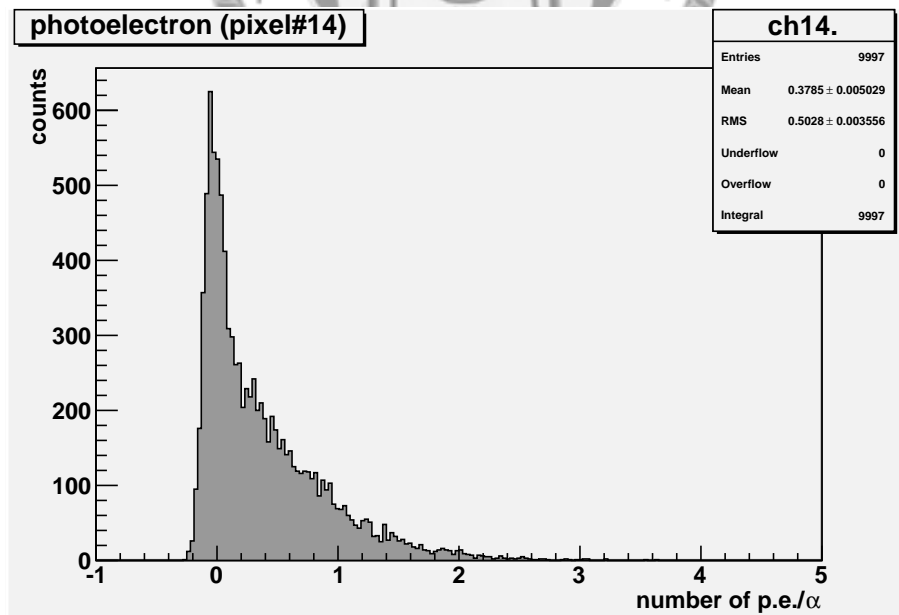Figure 6.2: Photoelectron distribution of triggered events

Figure 6.3: Photoelectron distribution of non-triggered events

And Fig. 6.3 shows photoelectron distribution of non-triggered events in one channel. The average photoelectrons of total non-triggered events is 0.297, the calculated photon flux is as following:

$$\phi_{photon} = \frac{0.297 \times 1.612}{200} \times \frac{1}{0.24} \times \frac{1}{0.766} \times \frac{1}{0.80} \times \frac{1}{0.56^2\pi} \times \frac{1}{(0.5°)^2}$$

$$= 106.4 m^{-2} sr^{-1} ns^{-1}$$

(6.3)

6.3 Conclusion

The value of Eq. 6.2 is overestimated because it means the average photons of over threshold events and the value of Eq. 6.3 is underestimated because it doesn't include over threshold events. But the photon flux of night sky background is expected to be close to value of Eq. 6.3 because trigger events are rare in whole measurement period (about $\frac{2}{100000}$). In conclusion, we had estimated the photon flux of night sky background in Mei-Fong is about $100 m^{-2} sr^{-1} ns^{-1}$.
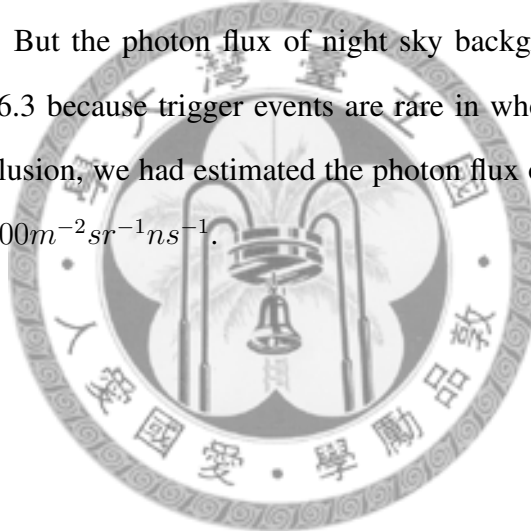
Chapter 7

Conclusion

The purpose of NuTel is to detect the tau neutrino ν_τ. It needs a large field of view and fast electrics to catch photons that are within few nano-second duration. The calibration of MAPMT will directly affect the result of measurement.

Even though the photoelectron peaks are not separated with Hamamatsu MAPMT H8500C, we have three ways to measure gain and number of photoelectron. With another photon detector – HPD, the measurement of calibration was confirmed.

We can calibrate one MAPMT, which has 64 pixels, at the same time by using LED to simulate the uniform light in a black box. The maximum ratio of anode output is about 3:1, and the dynamic range of digital potentiometer is about 4:1. As a result, the potentiometer can lessen the non-uniformity of MAPMT.

In July 2009, the first NuTel field test was carried out in Mei-Fong. The night sky background also had been estimated.

Until now, the calibrations of the electronics in NuTel have done. In the Future, the coincidence of two telescopes can be operated. The background can be eliminated then we can get more precise shower direction.

Bibliography

[1] B.R. Martin and G. Shaw. *Particle physics*. The Manchester physics series. J. Wiley, 1997.

[2] S Pakvasa. Neutrino decays and neutrino telescopes. page 10, 2003.

[3] George W. S. Hou and M. A. Huang. Expected performance of a neutrino telescope for seeing agn/gc behind a mountain. 2002.

[4] Ping Yeh, Koji Ueno, Yankun Chi, Y. Velikzhanin, Min-Zu Wang, Jing-Ge Shiu, and Chino-Cheng Hsu. The nutel telescope for observing very high energy tau neutrinos from agn. In *Nuclear Science Symposium Conference Record, 2003 IEEE*, volume 1, pages 139 – 143 Vol.1, 2003.

[5] Shiang-Rung Tsai. Estimation of the sensitivity of neutrino telescope (nutel). Master's thesis, National Taiwan University, 2005.

[6] Teng-Chieh Kang. Optical system of neutrino telescope. Master's thesis, National Taiwan University, June 2007.

[7] Eugene Hecht. *Optics*. Addison Wesley, 4th edition, August 2001.

[8] HAMAMATSU PHOTONTCS K. K. Editorial Committee. *PHOTOMULTIPLIER TUBES Basics and Applications*. HAMAMATSU PHOTONTCS K. K., third edition, February 2006.

[9] HAMAMATSU PHOTONTCS K. K. *FLAT PANEL TYPE MULTIANODE PHO-TOMULTIPLIER TUBE ASSEMBLY H8500 SERIES*, 2007.

[10] Kun-Xian Huang. Front-end readout system of neutrino telescope. Master's thesis, National Taiwan University, June 2007.

[11] Louis Lyons. *Statistics for Nuclear and Particle Physicists*. Cambridge University Press, 1989.

[12] K. Hoepfner, A. Skiba, and C. Hensel. Analysis of light-yield spectra observed with multi-anode pmt and hpd. *Nuclear Instruments and Methods in Physics Research Section A: Accelerators, Spectrometers, Detectors and Associated Equipment*, 483(3):747 – 757, 2002.

[13] D. L. Fried. Noise in photoemission current. *Appl. Opt.*, 4(1):79–80, Jan 1965.

[14] R. Foord, R. Jones, C. J. Oliver, and E. R. Pike. The use of photomultiplier tubes for photon counting. *Appl. Opt.*, 8(10):1975–1989, Oct 1969.

[15] E.H. Bellamy, G. Bellettini, J. Budagov, F. Cervelli, I. Chirikov-Zorin, M. Incagli, D. Lucchesi, C. Pagliarone, S. Tokar, and F. Zetti. Absolute calibration and monitoring of a spectrometric channel using a photomultiplier. *Nuclear Instruments and Methods in Physics Research Section A: Accelerators, Spectrometers, Detectors and Associated Equipment*, 339(3):468 – 476, 1994.

[16] Ping-Jung Su. Calibration of light measurement of the neutrino telescope (nutel). Master's thesis, Institute of Astrophysics, Department of Physics, National Taiwan University, Jul 2005.

[17] P. Adamson, G. Crone, L. Jenner, R. Nichol, R. Saakyan, C. Smith, J. Thomas, M. Kordosky, K. Lang, P. Vahle, A. Belias, T. Nicholls, G. Pearce, D. Petyt, M. Barker, A. Cabrera, J. Hartnell, P.S. Miyagawa, N. Tagg, A. Weber, E. Falk Harris, P.G. Harris, R. Morse, P. Symes, D. Michael, P.J. Litchfield, R. Lee, and

S. Boyd. The minos calibration detector. *Nuclear Instruments and Methods in Physics Research Section A: Accelerators, Spectrometers, Detectors and Associated Equipment*, 556(1):119 – 133, 2006.

[18] R. Dossi, A. Ianni, G. Ranucci, and O. Ju. Smirnov. Methods for precise photoelectron counting with photomultipliers. *Nuclear Instruments and Methods in Physics Research Section A: Accelerators, Spectrometers, Detectors and Associated Equipment*, 451(3):623 – 637, 2000.

[19] R. Nichol. *Calibration of the MINOS Detectors*. PhD thesis, University College London, Oct 2003.

[20] I. Chirikov-Zorin, I. Fedorko, A. Menzione, M. Pikna, I. S©kora, and S. Tok嫫. Method for precise analysis of the metal package photomultiplier single photoelectron spectra. *Nuclear Instruments and Methods in Physics Research Section A: Accelerators, Spectrometers, Detectors and Associated Equipment*, 456(3):310 – 324, 2001.

[21] *HIGH SPEED COMPACT HPD (Hybrid Photo-Detector) R10467U SERIESHIGH SPEED COMPACT HPD (Hybrid Photo-Detector) R10467U SERIES*, 2008.

[22] A. Fukasawa, J. Haba, A. Kageyama, H. Nakazawa, and M. Suyama. High speed hpd for photon counting. *Nuclear Science, IEEE Transactions on*, 55(2):758–762, April 2008.

[23] Chun-Lin Li. Integration of neutrino telescope and night sky background measurement. Master's thesis, National Taiwan University, Jan 2011.